

Harnessing Viscous Flow to Simplify the Actuation of Fluidic Soft Robots

Nikolaos Vasios,¹ Andrew J. Gross,¹ Scott Soifer,¹ Johannes T.B. Overvelde,⁴ and Katia Bertoldi¹⁻³

Abstract

Soft robots powered by pressurized fluid have recently enabled a variety of innovative applications in areas as diverse as space exploration, search and rescue systems, biomimetics, medical surgery, and rehabilitation. Although soft robots have been demonstrated to be capable of performing a number of different tasks, they typically require independent inflation of their constituent actuators, resulting in multiple input lines connected to separate pressure supplies and a complex actuation process. To circumvent this limitation, we embed the actuation sequencing in the system by connecting fluidic actuators with narrow tubes to exploit the effects of viscous flow. We developed modeling and optimization tools to identify optimal tube characteristics and we demonstrate the inverse design of fluidic soft robots capable of achieving a variety of complex target responses when inflated with a single pressure input. Our study opens avenues toward the design of a new generation of fluidic soft robots with embedded actuation control, in which a single input line is sufficient to achieve a wide range of functionalities.

Keywords: inverse design, viscous flow, fluidic soft actuators, simple actuation

Introduction

SOFT ROBOTS COMPRISING several inflatable actuators made of compliant materials have drawn significant attention over the past few years because of their ability to produce complex and adaptive motions through nonlinear deformation.¹⁻¹¹ The simplicity of their design, ease of fabrication, and low cost sparked the emergence of soft robots capable of walking,¹² crawling,¹³ camouflaging,¹⁴ assisting humans in grasping,^{15,16} and whose response can be further enhanced by exploiting elastic instabilities.^{17,18} However, to achieve a particular function, existing fluidic soft robots typically require multiple input lines, since each actuator must be inflated and deflated independently according to a specific preprogrammed sequence (Fig. 1a).

In an effort to reduce the number of input lines required for actuation, band-pass valves have been designed, which can address multiple actuators individually using a single modulated source of pressure.¹⁹ Another interesting avenue to reduce the number of required input signals is the direct exploitation of

the highly nonlinear behavior of the system without the introduction of additional stiff elements. To this end, it has been shown that a segmented soft actuator reinforced locally with optimally oriented fibers can achieve complex configurations upon inflation with a single input source.²⁰ Furthermore, the nonlinear properties of flexible two-dimensional metamaterials have been proven effective in reducing the complexity of the required input signal.^{13,21}

In this study, motivated by these opportunities for simplified actuation through nonlinearities, we focus on a system comprising an array of fluidic actuators interconnected through tubes and demonstrate that viscous flow in the tubes can be harnessed to achieve a wide variety of target responses through a single input (Fig. 1b). Although recent experiments with poroelastic soft actuators indicate that viscous flow is a promising candidate to simplify the actuation of soft robots,²² the highly nonlinear response of the system prohibits the identification of simple rules to guide its design. It is, therefore, crucial to implement robust algorithms to efficiently identify the system parameters resulting in the desired response.

¹John A. Paulson School of Engineering and Applied Sciences, Harvard University, Cambridge, Massachusetts.

²Wyss Institute for Biologically Inspired Engineering, Harvard University, Cambridge, Massachusetts.

³Kavli Institute for Bionano Science and Technology, Harvard University, Cambridge, Massachusetts.

⁴AMOLF, Amsterdam, The Netherlands.

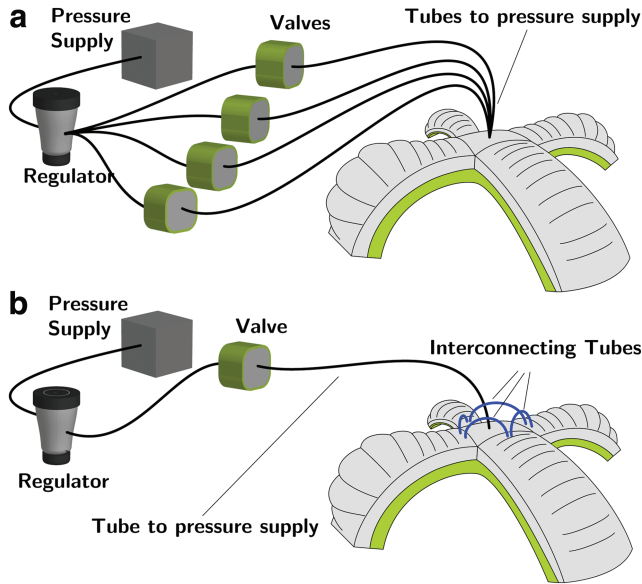


FIG. 1. Simplifying the actuation of fluidic soft robots. **(a)** Each actuator is typically inflated and deflated independently and individually, requiring a complex actuation process. **(b)** In this study, we exploit viscous flow in the tubes interconnecting the constituent actuators to design soft robots capable of achieving a variety of responses when inflated with a single pressure input. Color images are available online.

To this end, we first derive a model that accurately captures the viscous flow in the tubes and then combine the model with optimization to determine through inverse design the characteristics of the tubes leading to desired responses using a single input. The excellent agreement between experiments and simulations for a wide range of prescribed target responses demonstrates the robustness of our strategy. Finally, we show that our approach enables the realization of fluidic soft robots that can perform complex tasks when powered by a single pressure input, as demonstrated through the design of a simply actuated four-legged walker.

Fluidic Bending Actuators

Although the principles proposed in this study are applicable to systems comprising any fluidic soft actuator, to demonstrate the concept, we focus on fluidic bending actuators with an embedded network of channels and chambers.² All actuators have length $l = 75\text{mm}$ and a rectangular cross section $(w_c + 4t) \times (h + 3t)\text{mm}^2$, where $w_c = 16.5\text{mm}$ is the chamber width, $h = 7.5\text{mm}$ is the chamber height, and $t \in [1.5, 4]\text{mm}$ corresponds to the thickness of the top layer but also affects all other dimensions (Supplementary Table S1 and Supplementary Figures S1–S6). Moreover, the actuators contain eight identical chambers connected through narrow channels and are realized using two silicone rubbers with different stiffness (Fig. 2a; Supplementary Data).

The geometry of the embedded chambers as well as the contrasting properties of the two elastomers causes these actuators to progressively bend upon inflation in quasi-static conditions (Fig. 2b, c). Although the relationship between the bending curvature κ and the supplied volume Δv is almost linear (Fig. 2d; Supplementary Movie S1), their pressure–volume response is highly nonlinear and features a pressure

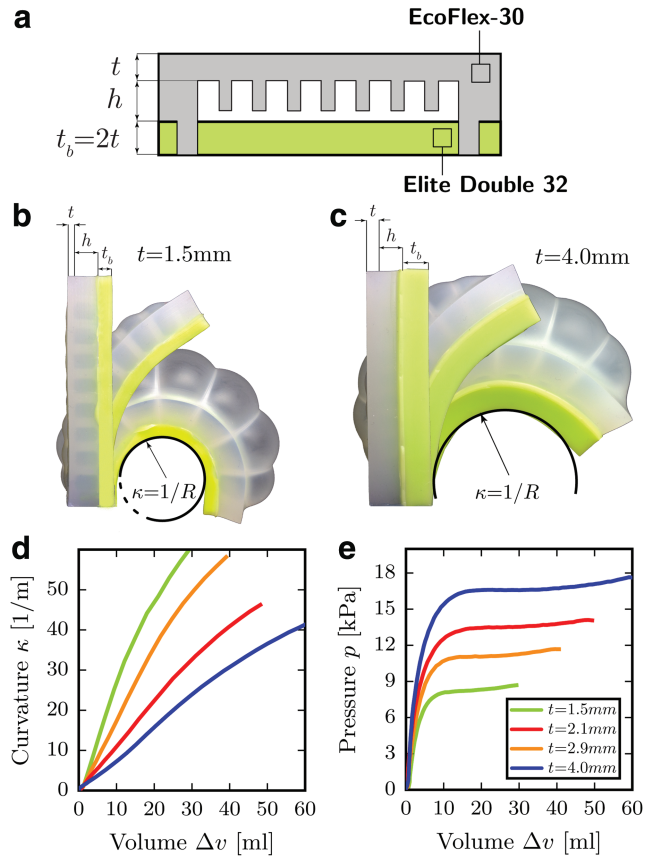


FIG. 2. Fluidic bending actuators. **(a)** Schematic of the cross section of a fluidic bending actuator. The two different elastomers used to fabricate the sample, Ecoflex-30 (Smooth-On, Inc.) and Elite Double 32 (Zhermack), are shown in *gray* and *green*, respectively. **(b, c)** Snapshots of fluidic bending actuators characterized by **(b)** $t = 1.5\text{mm}$ and **(c)** $t = 4.0\text{mm}$ at different actuation pressures. **(d)** Experimental curvature–volume curves for four actuators characterized by $t = 1.5, 2.1, 2.9,$ and 4.0mm . **(e)** Experimental pressure–volume curves for four actuators characterized by $t = 1.5, 2.1, 2.9,$ and 4.0mm . Color images are available online.

plateau (Fig. 2e; Supplementary Movie S1) caused by the reduction in stiffness associated with the ballooning of the top layer. Our results indicate that higher values of t lead to actuators that are simultaneously stiffer and harder to bend.

Harnessing Viscous Flow in the Tubes

Having characterized the quasi-static response of the fluidic bending actuators, we next investigate the response of the elementary system comprising two actuators connected by a tube (Fig. 3a).

To begin with, we consider two identical actuators with $t = 4\text{mm}$, connect one of them (Actuator 1, shown in blue in Fig. 3a) to the pressure source using a tube with length $L_1 = 10\text{cm}$ and internal radius $R_1 = 0.38\text{mm}$, and then connect Actuator 2 to Actuator 1 through a tube with length $L_2 = 10\text{cm}$ and internal radius $R_2 = 0.79\text{mm}$ (Fig. 3c, Supplementary Figures S7–S8). Upon supplying the system with air pressurized at $p_{input} = 60\text{kPa}$ for $t_{input} = 2.5\text{s}$ (Fig. 3c), the two actuators bend simultaneously, reach the same maximum bending curvature $\kappa_{1,max} = \kappa_{2,max} \simeq 40\text{m}^{-1}$ at $t = 2.5\text{s}$

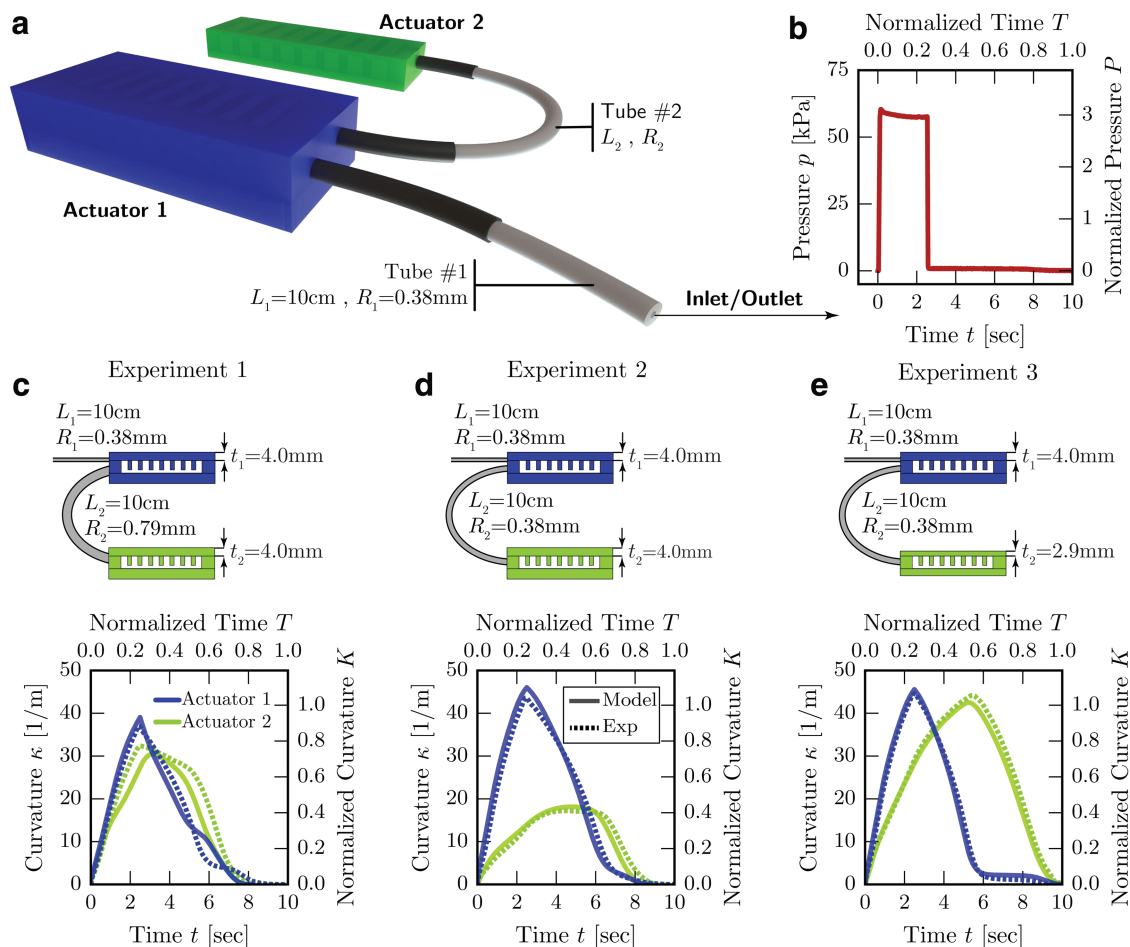


FIG. 3. Harnessing viscous flow in the tubes. **(a)** Schematic of the system considered in all three experiments. Tube 1 connects the input pressure to the first actuator, whereas Tube 2 connects the two actuators. Tube 1 has length $L_1 = 10\text{ cm}$ and radius $R_1 = 0.38\text{ mm}$ in all three experiments. **(b)** The rectangular pressure pulse used in all three experiments supplies $p_{input} = 60\text{ kPa}$ for $t_{input} = 2.5\text{ s}$. For $t > t_{input}$, $p_{input} = 0\text{ kPa}$ and Tube 1 acts as an outlet for the system to reset/deflate. **(c–e)** Schematics of the configuration tested in the three different experiments (top) and corresponding curvature responses for the two actuators (bottom). Color images are available online.

(Fig. 3f; Supplementary Movie S2), and then deflate through the inlet (since $p_{input} = 0\text{ kPa}$ for $t \geq t_{input}$, converting the inlet to an outlet for the system to reset). Note that by changing p_{input} and t_{input} , we are able to control the maximum curvature of the actuators. However, since in this system the tube used to connect the two actuators does not impose significant restrictions to the fluid flow, the two actuators will always bend simultaneously.

In an effort to investigate how viscous effects in the tubes can be harnessed to tune the rate of inflation of each actuator, we replace the interconnecting tube with a narrower tube, characterized by $R_2 = 0.38\text{ mm}$ (keeping $L_2 = 10\text{ cm}$; Fig. 3d). The experimental results shown in Figure 3d indicate that the actuators now bend at different rates and achieve the maximum curvature at different times (Supplementary Movie S3). However, we also find that $\kappa_{2,max}$ is significantly reduced due to energy losses associated with the viscous flow in the newly introduced interconnecting narrow tube and that $\kappa_{1,max}$ is increased because of the restriction on fluid flow imposed by such a tube.

To compensate for the energy loss, we replace the second actuator in our system with a more compliant actuator characterized by $t = 2.97\text{ mm}$ (Fig. 3e). In this case, the two actu-

ators still bend at different rates, but reach the same maximum bending curvature $\kappa_{1,max} = \kappa_{2,max} \simeq 45\text{ m}^{-1}$ (Fig. 3e; Supplementary Movie S4). Therefore, our simple experiments indicate that by carefully selecting both the fluidic actuators and the tubes, we can tune the bending rate as well as the maximum bending curvature of the actuators. However, the highly nonlinear response of the system prohibits the direct identification of simple rules that relate its parameters to specific desired responses. To design systems capable of achieving a target response, we first derive a model that describes their behavior and then solves the inverse problem to determine the system parameters that give rise to the target response.

Forward Modeling

Since our system comprises several fluidic bending actuators connected through narrow tubes, to predict its response we need to be able to capture the behavior of the actuators and determine the amount of fluid transferred through the tubes (Supplementary Figures S9–S11 and Supplementary Table S2). To this end, we focus on the $[i]$ -th tube in the system, which has length L_i (Fig. 4a), circular cross section with radius R_i (with

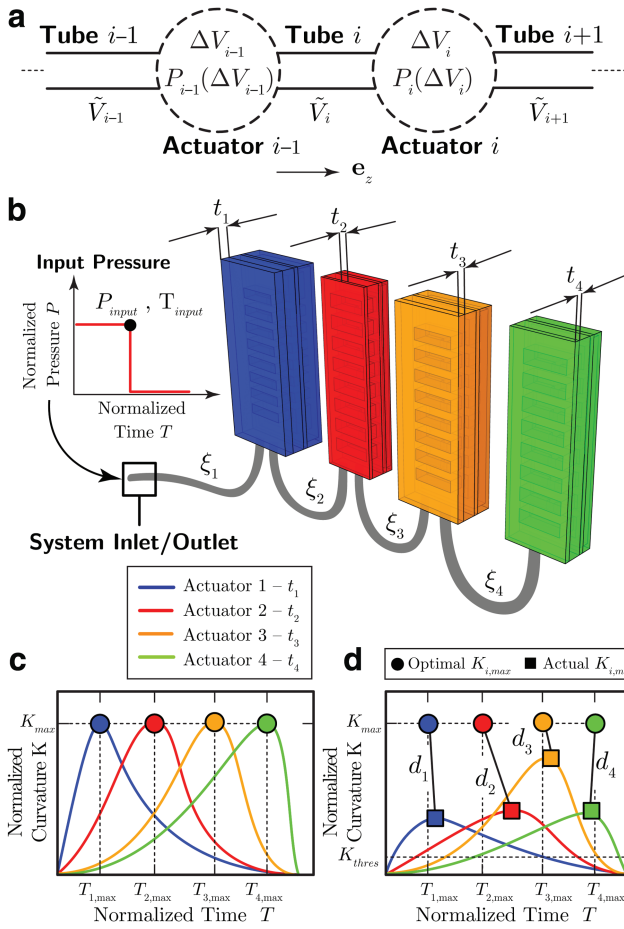


FIG. 4. Forward and inverse modeling. **(a)** Schematic of the system. The $[i]$ -th tube is connected to the $[i-1]$ -th and $[i]$ -th actuators. **(b)** Schematic of the configuration considered in the inverse problem, consisting of four fluidic bending actuators with thickness $t = 4.0, 2.9, 2.1,$ and 1.5 mm connected through narrow tubes and inflated by a rectangular pressure pulse. **(c)** The target response requires the $[i]$ -th actuator in the array to attain a maximum bending curvature of $K_{i,max}$ at a predefined time $T_{i,max}$ and then to completely deflate. **(d)** Parameters introduced to construct the objective function. Color images are available online.

$L_i \gg R_i$), and assume that (a) the tube is rigid and not deformed by the flow; (b) the head losses due to friction at the connections between the tube and the actuators can be captured by adjusting its length to $L_{i,eq}^{23}$; (c) the flow is incompressible and laminar; and (d) the fluid velocity has the form

$$\mathbf{u} = -\frac{2}{\pi R_i^2} \frac{d\tilde{v}_i}{dt} \left[\left(\frac{r}{R_i} \right)^2 - 1 \right] \mathbf{e}_z, \quad (1)$$

where $\tilde{v}_i = \int_0^t \int_0^{R_i} \mathbf{u} \cdot \mathbf{e}_z 2\pi r dr dt$ denotes the amount of fluid exchanged through the $[i]$ -th tube up to time t , and \mathbf{e}_z identifies the tangent vector to the tube (Supplementary Data).

Under these assumptions, integration of the Navier–Stokes equations over the volume of the tube yields

$$L_{i,eq} \frac{d^2 \tilde{v}_i(t)}{dt^2} = -\frac{\pi R_i^2}{\rho} (p_i - p_{i-1}) - \frac{8\mu L_{i,eq}}{R_i^2} \frac{d\tilde{v}_i(t)}{dt}, \quad (2)$$

where p_i is the pressure inside the $[i]$ -th actuator and μ is the dynamic viscosity of the fluid. Since for narrow tubes with $L_i \gg R_i$, as those considered in this study, the inertia term is negligible (Supplementary Data), Equation (2) can be rewritten in dimensionless form as

$$\frac{d\tilde{V}_i(t)}{dT} + \xi_i (P_i - P_{i-1}) = 0, \quad (3)$$

with

$$\xi_i = \frac{\pi G R_i^4 t_{max}}{8\mu v_0 L_{i,eq}}, \quad (4)$$

where $\tilde{V}_i = \tilde{v}_i/v_0$, $P_i = p_i/G$, and $T = t/t_{max}$ are the normalized fluid volume exchanged, pressure, and time, respectively (v_0 , G , and t_{max} denoting the volume of the smallest actuator in the system, the shear modulus of the material used to fabricate the actuators, and the response time of the system, respectively). Finally, since the normalized change in volume for the $[i]$ -th actuator, $\Delta V_i = \Delta v_i/v_0$, can be expressed in terms of the volumetric flows exchanged through the two tubes connected to it as

$$\Delta V_i = \tilde{V}_i - \tilde{V}_{i+1}, \quad (5)$$

Equation (3) can be rewritten as

$$\frac{d\Delta V_i(t)}{dt} + \xi_i (P_i - P_{i-1}) - \xi_{i+1} (P_{i+1} - P_i) = 0, \quad (6)$$

where the pressure inside the $[i]$ -th actuator, P_i , is a function of ΔV_i . For a system comprising N fluidic actuators interconnected through narrow tubes, Equation (6) defines a system of N coupled differential equations, which, given a pressure–volume relationship for the actuators, can be solved numerically to determine the normalized change in volume for the $[i]$ -th actuator as a function of time (Supplementary Data). Once the volume history for all actuators is known, their bending curvature is determined using the corresponding curvature–volume relationship.

To verify the validity of our model, we numerically integrate Equation (6) using the pressure–volume and curvature–volume relations of Figure 2d and e to simulate the experiments reported in Figure 3. We find that our numerical model (solid lines) can successfully reproduce the responses observed in experiments (dashed lines) for all three systems considered in Figure 3. The capability of the numerical model to accurately capture the response of the system in configurations involving different tubes and actuators ensures that the model can be used to identify optimal configurations.

Inverse Design

Although Equation (6) can be used to predict the temporal response of arbitrary arrays of fluidic actuators connected through narrow tubes, in this study, we are mostly interested in the inverse problem of designing a system capable of achieving particular target responses (Supplementary Figures S12–S16).

Specifically, we focus on systems consisting of four fluidic bending actuators characterized by $t = 4.0, 2.9, 2.1,$ and 1.5 mm connected through narrow tubes (Fig. 4b) and want the $[i]$ -th actuator in the array to attain a maximum bending

curvature $K_{i, \max} = \kappa_{i, \max} / \kappa_{\text{ref}}$ ($\kappa_{\text{ref}} = \pi / l = 41.88 \text{ m}^{-1}$ being the curvature of a semicircle with arc length equal to the initial length l of the actuators) at a predefined time $T_{i, \max} = t_{i, \max} / t_{\max}$ and then to completely deflate (Fig. 4c).

Specifying a rectangular pulse for the input pressure (Fig. 4b), the parameters to be determined to achieve the target response are (a) the dimensionless tube parameters ξ_i (with $i = 1, 2, 3, 4$) that uniquely define the tube geometry, (b) the magnitude of the input pressure $P_{\text{input}} = p_{\text{input}} / G$, and (c) the pressurization time $T_{\text{input}} = t_{\text{input}} / t_{\max}$. To identify a set of such parameters resulting in the desired response, we minimize

$$\mathcal{Z} = \sum_{i=1}^4 (d_i + 0.25 \tau_i), \quad (7)$$

where τ_i denotes the amount of time that the $[i]$ -th actuator spends above a threshold curvature $K_{i, \text{thres}} = 0.05 K_{i, \max}$ and is introduced to ensure that the actuators quickly deflate after approaching the target point of maximum curvature. Moreover, d_i is the ‘‘distance’’ in the $K - T$ space between the target and actual points of maximum curvature for the $[i]$ -th bending actuator (Fig. 4d),

$$d_i = \sqrt{\Delta K_i^2 + \Delta T_i^2}, \quad (8)$$

with

$$\Delta K_i = K_{i, \max} - \max_T K_i(T), \quad (9)$$

$$\Delta T_i = T_{i, \max} - \operatorname{argmax}_T K_i(T). \quad (10)$$

$K_i = \kappa_i / \kappa_{\text{ref}}$ being the normalized curvature of the $[i]$ -th actuator.

Finally, we input our model Equation (6), the actuators’ behavior (Fig. 2d, e), and the objective function Equation (7) into a Python implementation of the covariance matrix adaptation evolution strategy algorithm²⁴ and solve the inverse problem (i.e., determine the parameters ξ_i , P_{input} , and T_{input} resulting in the target response) using a population size of 50, an initial standard deviation of 0.4, and a starting point that is randomly drawn from a standard normal distribution (Supplementary Data).

In Figure 5, we report results for two different target responses. First, we optimize the system so that all bending actuators achieve the same bending curvature $K_{i, \max} = 1.0$ at $T_{i, \max} = 0.1 + (i - 1)0.2$ (with $i = 1, 2, 3, 4$; Fig. 5a), targeting a bending sequence. The optimization algorithm converges to the optimal solution after 80 iterations (Fig. 5b) and indicates that, if we choose the response time to be $t_{\max} = 25$ s, the system most closely approaches the prescribed target when the tubes have length $(L_1, L_2, L_3, L_4) = (78.6, 10.0, 43.7, 122.4)$ cm and the input supplies $p_{\text{input}} = 102.7$ kPa for $t_{\text{input}} = 3.4$ s. As shown in Figure 5c, for this set of parameters, both the numerical model (solid lines) and the experimental observations (dashed lines) closely follow the target response, that is, the four actuators reach the specified maximum bending curvatures at the desired times (markers) and then deflate (Fig. 5d; Supplementary Movie S5).

Second, we look for a system in which $K_{i, \max} = 0.6 + 0.2(i - 1)$ and $T_{i, \max} = 0.15 + 0.1(i - 1)$ (with $i = 1, 2, 3, 4$),

so that the actuators sequentially bend with progressively increasing curvature (Fig. 5e). Our optimization algorithm converges to the optimal solution after 60 iterations (Fig. 5f) and finds that this response can be achieved for $(L_1, L_2, L_3, L_4) = (3.5, 3.0, 14.8, 43.0)$ cm with $p_{\text{input}} = 23.3$ kPa and $t_{\text{input}} = 5.8$ s. Remarkably, for this case we again find that both our experiments and simulations closely match the target response (Fig. 5f, g; Supplementary Movie S6).

We emphasize that both target responses shown in Figure 5 would require an independently controlled input line associated with each actuator in the array, if they were to be achieved without harnessing viscous effects in the fluidic network. Therefore, by carefully selecting the narrow tubes connecting the fluidic actuators as well as the input pressure and pressurization time, the target response for the system can be naturally embedded in its design, allowing for a substantial simplification in system actuation. Note that even though in Figure 5 we focus on two responses, our strategy is robust and can be used to achieve a wide variety of responses (Supplementary Data).

Finally, it is important to note that in cases where the careful selection of the narrow tubes, input pressure, and pressurization time through optimization lead to system responses that do not closely approach the objective, the solution space can be further enriched by further optimizing the geometry of the fluidic actuators (Supplementary Data). However, from a practical point of view, optimizing the geometry of the fluidic actuators is not always desirable, since it requires the fabrication of new actuators.

Multiobjective Optimization

The results of Figure 5 demonstrate the robustness of our approach in identifying systems capable of achieving a desired target response. However, in many cases, soft robots need to be able to achieve multiple different responses and easily switch from one to another. To this end, we investigate whether varying the magnitude of input pressure P_{input} and pressurization time T_{input} is sufficient to enable a single system to achieve more than one target responses. Performing a brute force search for the range of responses that a system optimized for a specific sequence can achieve just by varying P_{input} and T_{input} , we find that the inflation parameters have very little effect in changing the initial response for which the system was optimized (Supplementary Data and Supplementary Figure S17).

Therefore, to effectively identify a system capable of switching from one desired response (Target 1) to another (Target 2) just by varying the inflation parameters, we formulate a multiobjective optimization problem. The dimensionless tube parameters ξ_i (with $i = 1, 2, 3, 4$) and the inflation parameters associated with the two target responses [i.e., $(P_{\text{input}}^{(1)}, T_{\text{input}}^{(1)})$ and $(P_{\text{input}}^{(2)}, T_{\text{input}}^{(2)})$] are obtained by minimizing

$$\mathcal{Z} = \alpha \mathcal{Z}^{(1)} + (1 - \alpha) \mathcal{Z}^{(2)}, \quad (11)$$

where $\mathcal{Z}^{(1)}$ and $\mathcal{Z}^{(2)}$ are the objective functions corresponding to Targets 1 and 2 and $\alpha \in [0, 1]$ is a scalar weighing the relative importance of each objective.

Focusing on a system capable of switching between the two responses defined by the anchor points shown in Figure 6a and b, our optimization algorithm finds that both objectives are best approached for $\alpha = 0.5$ (Fig. 6c) when

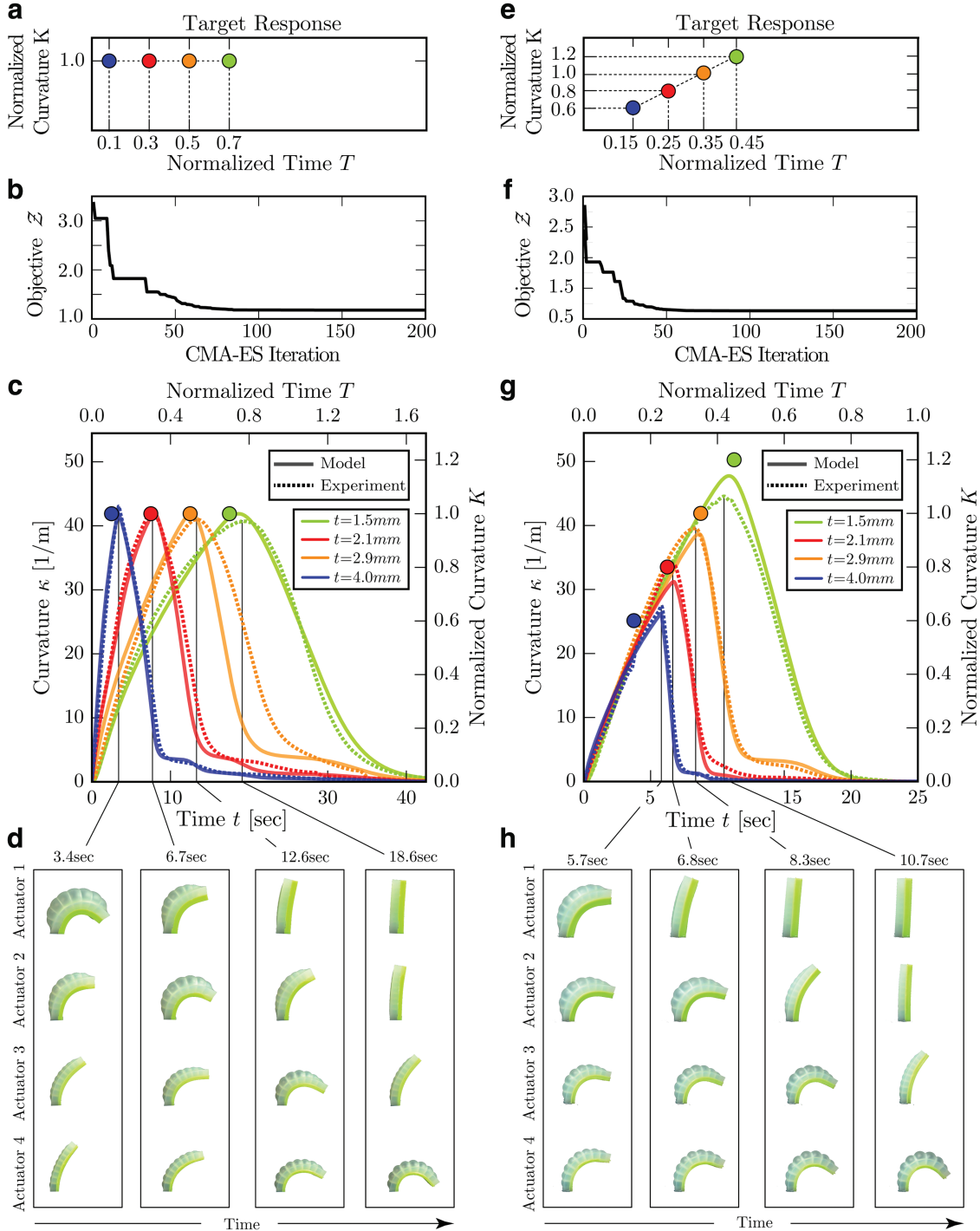


FIG. 5. Solution of the inverse problem. **(a)** The first target response requires all actuators in the system to achieve the same maximum bending curvature $K_{i,max} = 1.0$ but at different times $T_{i,max} = 0.1 + 0.2(i - 1)$ (with $i = 1, 2, 3,$ and 4). **(b)** Evolution of the objective function during CMA-ES iterations. **(c)** Curvature response for the optimal system, as determined from the numerical model (*solid lines*) and experiments (*dashed lines*). **(d)** Snapshots of the four actuators at $T = 0.13, 0.27, 0.5, 0.74$, corresponding to the times at which each actuator achieves its maximum curvature during the experiment. **(e)** The second target response requires all actuators in the system to achieve the maximum bending curvature $K_{i,max} = 0.6 + 0.2(i - 1)$ at $T_{i,max} = 0.15 + 0.1(i - 1)$ (with $i = 1, 2, 3,$ and 4). **(f)** Evolution of the objective function during CMA-ES iterations. **(g)** Curvature response for the optimal system, as determined from the numerical model (*solid lines*) and experiments (*dashed lines*). **(h)** Snapshots of the four actuators at $T = 0.23, 0.27, 0.33, 0.43$, corresponding to the times at which each actuator achieves its maximum curvature during the experiment. CMA-ES, covariance matrix adaptation evolution strategy. Color images are available online.

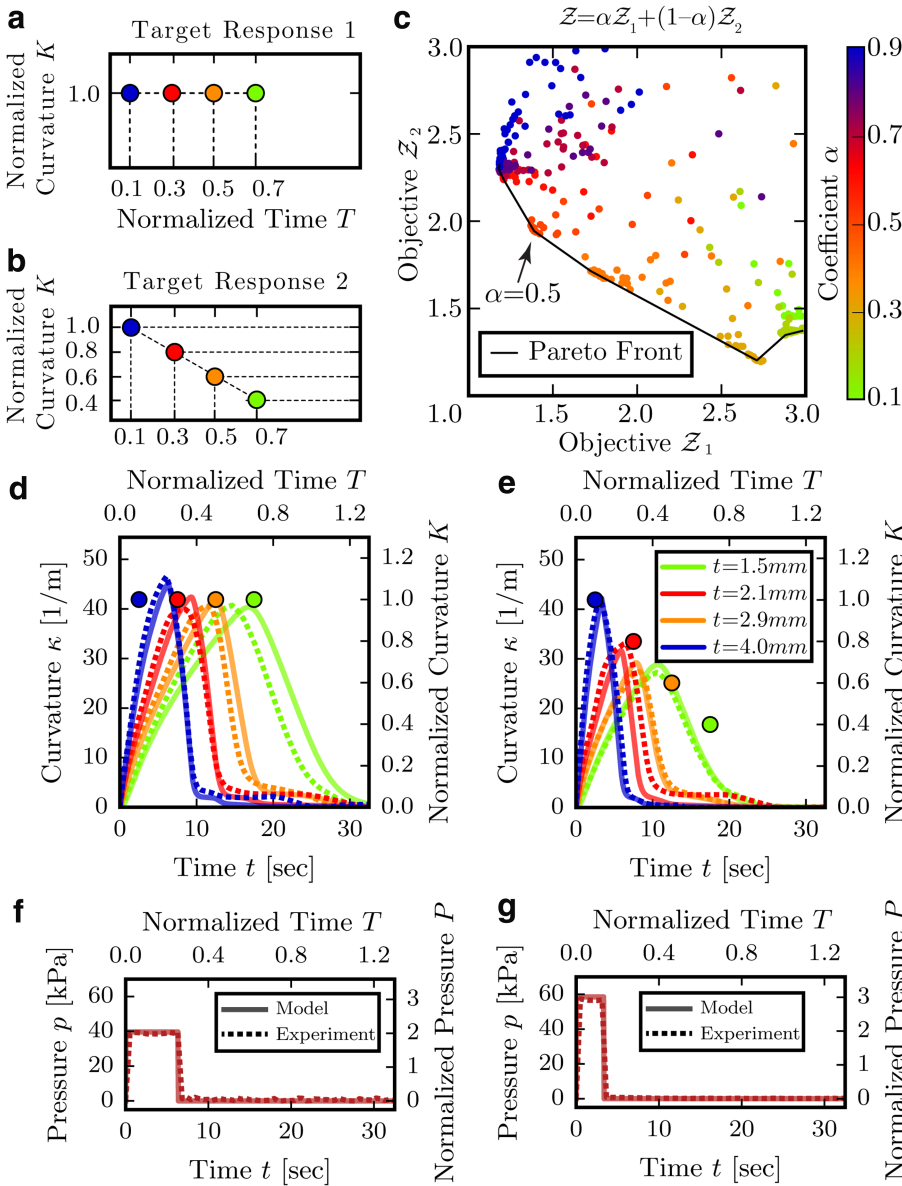


FIG. 6. Multiobjective optimization. **(a, b)** The curvature anchor points defining Target 1 **(a)** and Target 2 **(b)**, respectively. **(c)** Pareto front. The *black* line connects members of the Pareto set. The color of the markers corresponds to value of α used in the optimization. The overall optimal solution that most closely approaches both objectives is found for $\alpha = 0.5$. **(d, e)** Numerical (*solid lines*) and experimental (*dashed lines*) curvature responses for the optimal solution of the multiobjective inverse problem for Target 1 **(d)** and Target 2 **(e)**, respectively. **(f, g)** Input pressures required to achieve Target 1 **(f)** and Target 2 **(g)**, as determined from the solution of the multiobjective inverse problem (*solid lines*) and as provided in experiments (*dashed lines*). Color images are available online.

$(L_1, L_2, L_3, L_4) = (16.5, 10.0, 48.0, 124.0)$ cm, $p_{input}^{(1)} = 39.6$ kPa, $t_{input}^{(1)} = 6.32$ s, $p_{input}^{(2)} = 58.5$ kPa, and $t_{input}^{(2)} = 3.33$ s. The corresponding numerical (*solid lines*) and experimental (*dashed lines*) responses are again in excellent agreement for both system responses and come sufficiently close to both objectives (Fig. 6d, e; Supplementary Movie S7). Consequently, our multiobjective optimization approach can be used to successfully design systems that can achieve different target responses just by varying the input pressure magnitude P_{input} and duration T_{input} (Supplementary Figure S18).

Conclusions

In summary, using a combination of optimization tools and experiments, we have shown that viscous flow in the tubes interconnecting fluidic actuators can be exploited to design soft robots that, although inflated through a single input, are capable of achieving a wide range of target responses.

Throughout our study, we have found an excellent agreement between the numerical predictions and experimental findings—a clear indication of the predictive power and robustness of our framework. Even though in this work we focused on systems in which the actuators inflate according to a target sequence, we believe that our strategy can be directly applied to design a wide range of fluid-actuated soft robots capable of performing multiple different tasks using a single input.

To demonstrate how actuation sequencing through viscous flow can simplify the actuation of fluidic soft robots, we design a soft robot that comprises the four bending actuators considered throughout this study (with top layer thicknesses $t = 4.0, 2.9, 2.1$ and 1.5 mm), connect Actuator 1 ($t = 4.0$ mm) to the pressure input through a tube with $L_1 = 78.6$ cm and $R_1 = 0.38$ mm, and supply $p_{input} = 102.7$ kPa for $t_{input} = 3.4$ s. If the four actuators are interconnected using tubes that do not impose significant restrictions to fluid flow (i.e., $R_i = 0.79$ mm for $i = 2, 3, 4$), only the most compliant actuator inflates and no

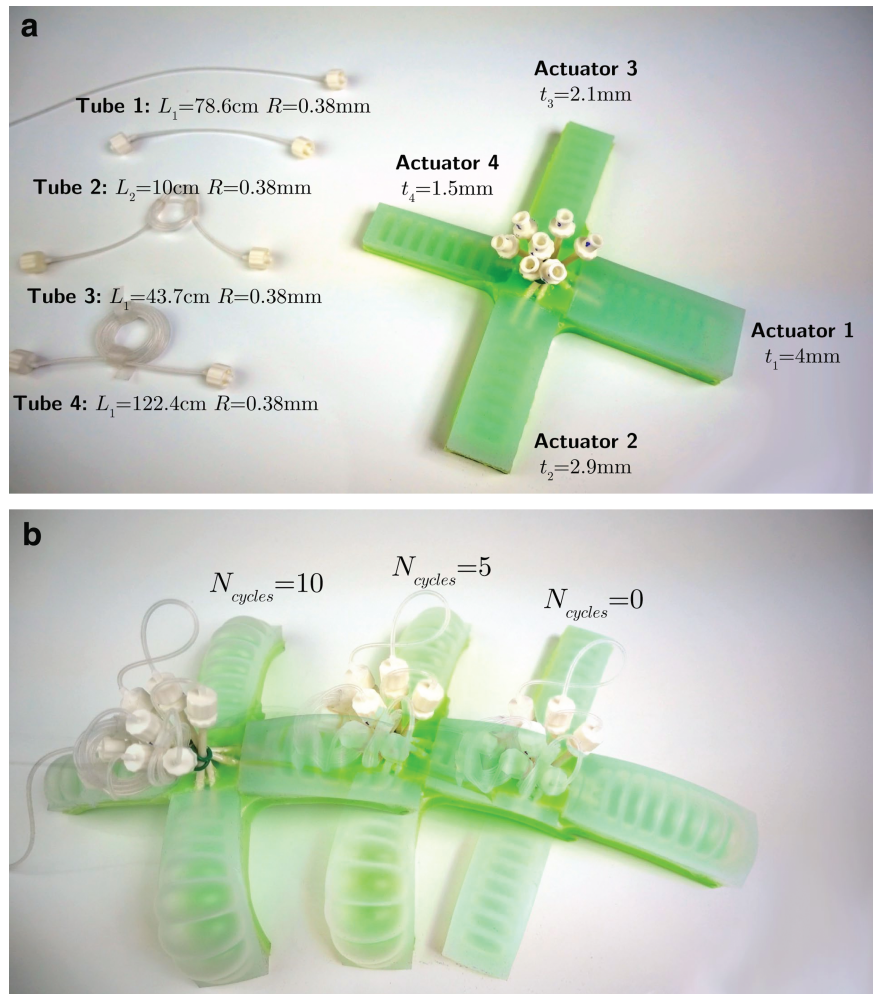


FIG. 7. Actuating a four-legged fluidic soft robot using a single pressure input. **(a)** The four actuators considered throughout this study are interconnected using narrow tubes with length (L_1, L_2, L_3, L_4) = (78.6, 10.0, 43.7, 122.4) cm and radius $R=0.38$ mm. Tube 1 is connected to a pressure input supplying the robot with $p_{input}=102.7$ kPa for $t_{input}=3.4$ s every 40 s. **(b)** Snapshots of the position of the soft robot after 5 and 10 inflation cycles, demonstrating its ability to walk in a predictable and consistent manner (Supplementary Movie S8). Color images are available online.

functionality is achieved (Supplementary Movie S8). In contrast, if the actuators are connected using the tube lengths that correspond to the optimal solution of Figure 5a and b (Fig. 7a), the soft robot walks in a consistent and predictable manner covering a distance of ≈ 15 cm for 10 inflation cycles (Fig. 7b; Supplementary Movie S8).

Finally, although in this study we only considered objectives for which a single curvature–time point was sufficient to describe the desired response of each actuator, one could differently focus on the smooth control of fluidic actuators and define an objective function in terms of multiple target points in the curvature–time space for each actuator. We expect that very few modifications would be necessary to achieve a smoother response for every actuator, since viscous flow is inherently a “smoothing” process.

Acknowledgment

This research was supported by the NSF under grant number DMR-1420570.

Authors' Contributions

N.V., J.T.B.O., and K.B. designed research; N.V. performed research; N.V., J.T.B.O., and K.B. analyzed data; N.V., A.J.G., and S.S. performed experiments; A.J.G. helped design experiments; and N.V. and K.B. wrote the article.

Author Disclosure Statement

The authors declare no conflict of interest.

Supplementary Material

Supplementary Data
 Supplementary Movie S1
 Supplementary Movie S2
 Supplementary Movie S3
 Supplementary Movie S4
 Supplementary Movie S5
 Supplementary Movie S6
 Supplementary Movie S7
 Supplementary Movie S8

References

1. Trivedi D, Rahn CD, Kier WM, *et al.* Soft robotics: Biological inspiration, state of the art, and future research. *Appl Bionics Biomech* 2008;5:99–117.
2. Ilievski F, Mazzeo AD, Shepherd RF, *et al.* Soft robotics for chemists. *Angew Chem Int Ed Engl* 2011;50:1890–1895.
3. Shepherd RF, Ilievski F, Choi W, *et al.* Multigait soft robot. *Proc Natl Acad Sci U S A* 2011;108:20400–20403.
4. Kim S, Laschi C, Trimmer B. Soft robotics: a bioinspired evolution in robotics. *Trends Biotechnol* 2013;31:287–294.

5. Carmel M. Soft robotics: A perspective—Current trends and prospects for the future. *Soft Robot* 2014;1:5–11.
6. Rus D, Tolley MT. Design, fabrication and control of soft robots. *Nature* 2015;521:467–475.
7. Laschi C, Mazzolai B, Cianchetti M. Soft robotics: Technologies and systems pushing the boundaries of robot abilities. *Sci Robot* 2016;1:eaah3690.
8. Zhao H, O'Brien K, Li S, *et al.* Optoelectronically innervated soft prosthetic hand via stretchable optical waveguides. *Sci Robot* 2016;1:eaai7529.
9. Dian Y, Verma MS, So JH, *et al.* Buckling pneumatic linear actuators inspired by muscle. *Adv Mater Technol* 2016;1:1600055.
10. Polygerinos P, Correll N, Morin SA, *et al.* Soft robotics: Review of fluid-driven intrinsically soft devices; manufacturing, sensing, control, and applications in human-robot interaction. *Adv Eng Mater* 2017;19:1700016.
11. Krishnan G, Bishop-Moser J, Kim C, *et al.* Kinematics of a generalized class of pneumatic artificial muscles. *J Mech Robot* 2015;7:041014.
12. Tolley MT, Shepherd RF, Mosadegh B, *et al.* A resilient, untethered soft robot. *Soft Robot* 2014;1:213–223.
13. Rafsanjani A, Zhang Y, Liu B, *et al.* Kirigami skins make a simple soft actuator crawl. *Sci Robot* 2018;3:eaar7555.
14. Morin SA, Shepherd RF, Kwok SW, *et al.* Camouflage and display for soft machines. *Science* 2012;337:828–832.
15. Polygerinos P, Wang Z, Galloway KC, *et al.* Soft robotic glove for combined assistance and at-home rehabilitation. *Robot Auton Syst* 2015;73:135–143.
16. Paoletti P, Jones GW, Mahadevan L. Grasping with a soft glove: Intrinsic impedance control in pneumatic actuators. *J Royal Soc Interface* 2017. [Epub ahead of print]; DOI: 10.1098/rsif.2016.0867.
17. Overvelde JTB, Kloek T, D'haen JJA, *et al.* Amplifying the response of soft actuators by harnessing snap-through instabilities. *Proc Natl Acad Sci U S A* 2015;112:10863–10868.
18. Rothmund P, Ainla A, Belding L, *et al.* A soft, bistable valve for autonomous control of soft actuators. *Sci Robot* 2018;3:eaar7986.
19. Napp N, Araki B, Tolley MT, *et al.* Simple passive valves for addressable pneumatic actuation. 2014 IEEE International Conference on Robotics and Automation (ICRA), Hong Kong, China, 2014, pp. 1440–1445.
20. Connolly F, Walsh CJ, Bertoldi K. Automatic design of fiber-reinforced soft actuators for trajectory matching. *Proc Natl Acad Sci U S A* 2017;114:51–56.
21. Yang D, Mosadegh B, Ainla A, *et al.* Buckling of elastomeric beams enables actuation of soft machines. *Adv Mater* 2015;27:6323–6327.
22. Futran CC, Ceron S, Murray BM, *et al.* Leveraging fluid resistance in soft robots. In: 2018 IEEE International Conference on Soft Robotics (RoboSoft). Livorno, Italy: IEEE, April 2018:473–478.
23. Menon E. *Piping Calculations Manual*. New York: McGraw-Hill Education, 2005.
24. Hansen N, Müller SD, Koumoutsakos P. Reducing the time complexity of the derandomized evolution strategy with Covariance Matrix Adaptation (CMA-ES). *Evol Comput* 2003;11:1–18.

Address correspondence to:
Johannes T.B. Overvelde
 AMOLF
 Science Park 104
 Amsterdam 1098XG
 The Netherlands

E-mail: overvelde@amolf.nl

Katia Bertoldi
 John A. Paulson School of Engineering
 and Applied Sciences
 Harvard University
 Cambridge, MA 02138

E-mail: bertoldi@seas.harvard.edu

Supporting Information

Nikolaos Vasios¹, Andrew J. Gross¹,
Scott Soifer¹, Johannes T. B. Overvelde^{4,*}, Katia Bertoldi^{1,2,3,*}

¹J. A. Paulson School of Engineering and Applied Sciences,
Harvard University, Cambridge, MA 02138, USA

²Wyss Institute for Biologically Inspired Engineering
Harvard University, Cambridge, MA 02138, USA

³Kavli Institute for Bionano Science and Technology
Harvard University, Cambridge, MA 02138, USA

⁴AMOLF, Science Park 104, 1098XG Amsterdam, The Netherlands

*To whom correspondence should be addressed;
E-mail: bertoldi@seas.harvard.edu or overvelde@amolf.nl

S1 Fluidic Bending Actuators

In this section we provide details on the design, fabrication, testing and modeling of the individual fluidic bending actuators considered in this study.

Design

Although the principles proposed in this study can be applied to any type of fluidic soft actuator, to demonstrate the idea we focus on fluidic bending actuators that consist of a network of channels and chambers embedded in an elastomer (PneuNets).² Specifically, we consider an actuator with initial length $l = 75$ mm and a rectangular cross section with width w and height h_{total} (see Fig. S1). Note that, since in this study the response

of the actuators is tuned by varying the thickness of the upper layer t (with $t \in [1.5, 4]$ mm), to make sure that all of them bend upon inflation both w and h_{total} depend on t with $w = 33 + 4t$ and $h_{\text{total}} = 7.5 + 3t$ (if the width and height of the actuator remain unchanged when t changes, the actuators corresponding to larger values of t will just expand and not bend, upon inflation).

To achieve bending upon inflation,

- (i) we embed eight chambers within the actuator, each with length $l_c = 4$ mm and width $w_c = 3$ mm connected via narrow channels with length $d_c = 3$ mm, width $w_t = 3$ mm and height $h_t = 1.875$ mm (see Fig. S1);
- (ii) we use two different elastomers to fabricate the actuator: a more compliant one for the top part (shown in gray in Fig. S1) and a stiffer one for the bottom part (shown in green in Fig. S1).

The values for all geometric parameters of the actuators modeled and fabricated in this study are summarized in Table S1. Finally, we point out that our design is fully-parameterized, so that the response of the actuators is unaffected (i.e. the normalized pressure-volume and normalized curvature-volume curves remain the same) if all the dimensions are scaled by the same factor.

Fabrication

The actuators tested in this study are made of silicone rubbers. Specifically, we used Ecoflex 00-30 (Smooth-On, Inc.) for the top (shown in gray in Fig. S1) and Elite Double 32 (Zhermack) for the bottom (shown in green in Fig. S1). The two layers were casted and joined together using the 3-part mold shown in Fig. S2. The mold was designed in Solidworks and 3d printed in Vero-blue using an Objet Connex 500 printer (Stratasys).

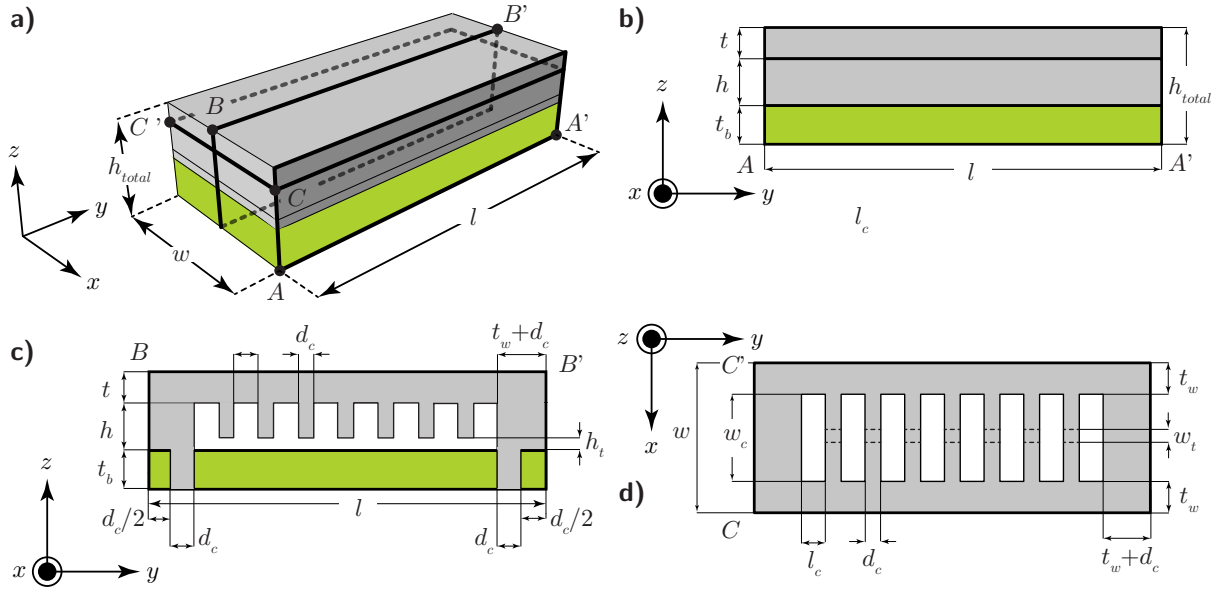


Figure S1: 3D model of the bending actuator considered in this study. (a) Isometric view. Note that the gray and green regions correspond to EcoFlex-30 (Smooth-On, Inc.) and Elite Double 32 (Zhermack) respectively. (b) Side view highlighting the top and bottom layer thickness. (c) Side cross-section highlighting the details of the inner chambers and channels. (d) Top cross-section highlighting the details of the inner chambers and channels.

Table S1: Geometric parameters of the actuators considered in this study

Geometric parameter	Value
Actuator Length, l	75 mm
Chamber Height, h	7.5 mm
Chamber Width, w_c	16.5 mm
Number of Chambers, n	8 mm
Chamber Distance, d_c	3.0 mm
Channel Height, $h_t = h/4$	1.875 mm
Channel Width, $w_t = w_c/5.5$	3.0 mm
Top Layer Thickness, t	1.5 – 4.0 mm
Bottom Layer Thickness, $t_b = 2t$	3.0 – 8.0 mm
Wall Thickness, $t_w = 2t$	3 – 8.0 mm
Actuator Width, $w = 2w_c + 2t_w$	36.0 – 41.0 mm
Chamber Length, $l_c = [l - 2t_w - (n + 1)d_c]/n$	5.25 – 4.0 mm

Parts I and II slide into one another and were used to cast the top portion of the actuator made of EcoFlex-30. Part III was used to cast the bottom layer of the actuator made of Elite Double 32.

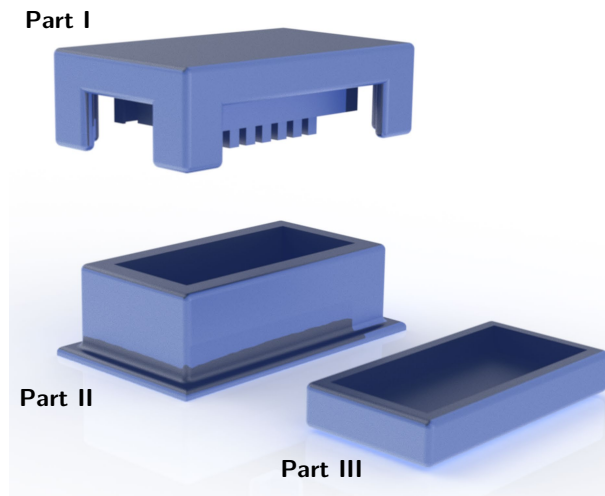


Figure S2: A 3D render of Parts I, II and III of the mold used to cast our fluidic bending actuators.

Our actuators can be fabricated using the following 12 steps (see Fig. S3):

Step 1: expose all inner surfaces of the mold to Ease Release 200 spray (Mann Release Technologies) to facilitate the process of removing the cured elastomer later on;

Step 2: prepare EcoFlex-30 by (a) dispensing equal amount of part A and B in a clean container, (b) mixing thoroughly and (c) vacuum degassing for about 10 minutes.

Step 3: pour the Ecoflex mixture inside part II of the mold.

Step 4: slowly place part I of the mold on top of part II, while allowing for any excess silicone to flow out of the mold.

Step 5: cure the EcoFlex for about 4 to 5 hours at room temperature, while securing a tight seal between mold parts I and II.

Step 6: (a) remove the cured EcoFlex from the mold and (b) trim any protruding edges (if necessary).

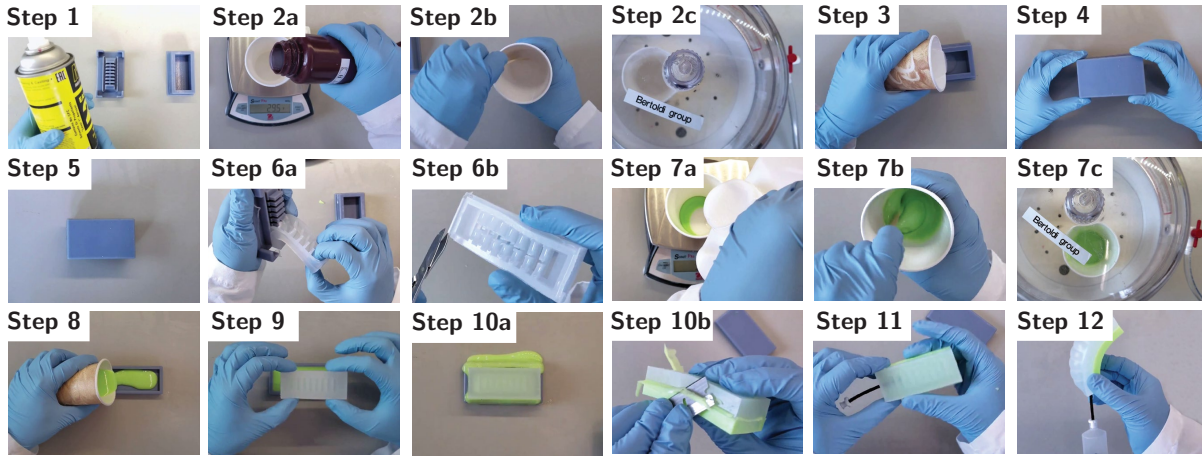


Figure S3: Snapshots of the 12 steps required for the fabrication of our fluidic bending actuators

Step 7: prepare Elite Double 32 by (a) dispensing an equal amount of base and catalyst in a clean container, (b) mixing thoroughly and (c) vacuum degassing for about 3 minutes.

Step 8: pour the Elite Double 32 mixture inside part III of the mold.

Step 9: carefully place the EcoFlex-30 part of the actuator on top of the liquid Elite Double 32 and allow the latter to cure for about 25 minutes and bond to the EcoFlex.

Step 10: remove the cured actuator from part III of the mold and trim any protruding edges if necessary.

Step 11: insert a tube in one end of the actuator

Step 12: test the fabricated actuator for any leaks by inflating with a syringe pump. If leaks are present, patch them using the appropriate silicone rubber.

Testing

In order to fully characterize the quasi-static response of the fabricated bending actuators we conducted experiments to determine their pressure-volume and curvature-volume relationships. Note that as a part of this study we fabricated and tested actuators with

four different values of the top layer thickness, namely $t = 1.5, 2.1, 2.9$ and 4.0 mm. All the actuators were tested using a syringe pump (Standard Infuse/Withdraw PHD Ultra; Harvard Apparatus) equipped with two 50-mL syringes (1000 series, Hamilton Company) with an accuracy of $\pm 0.1\%$.

Pressure-Volume

For the pressure-volume measurements the actuators were inflated using water (to avoid effects of air compressibility) at a rate of 50ml/min, ensuring quasi-static conditions. The pressure inside the actuators was measured during inflation using a MPX5050DP (NXP USA Inc.) pressure sensor, connected to an Arduino Nano. The Arduino was able to log the pressure in a text file with the use of a Python script and the serial module.

In Fig. S4 we report the evolution of the pressure p as a function of the volume change Δv inside the actuator for all actuators tested in this study¹. The results of Fig. S4 show that the pressure-volume curves for all actuators are nonlinear and feature a pressure plateau. The plateau indicates the maximum pressure that the given actuator can withstand and can be tuned by varying t (i.e. it monotonically increases with t).

Curvature-Volume

For the curvature measurements all actuators were inflated with air (the use of water for inflation was avoided to eliminate the influence of gravitational effects on the curvature of the actuators). Upon inflation, we recorded videos of the deformation of each actuator, which we processed to extract the curvature. Specifically, for each recorded frame we identified the bottom edge of the actuator (highlighted in red in Fig. S5b) using a Python image processing script. We then determined the radius R of the circle that best fits

¹Note that the curves reported in Fig. S4 were determined by averaging the pressure volume curves from 4 inflation cycles per actuator

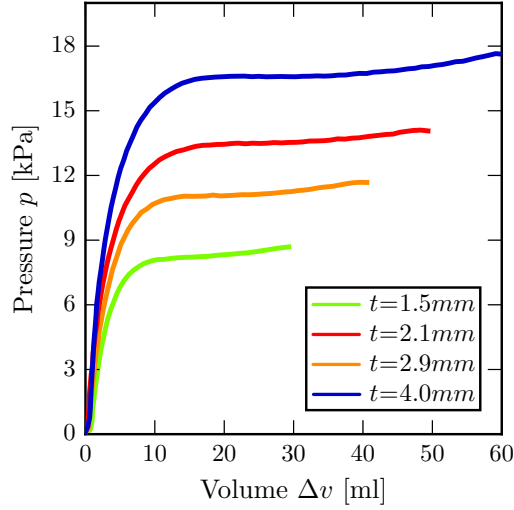


Figure S4: Experimental pressure-volume curves for four actuators characterized by $t = 1.5, 2.1, 2.9$ and 4.0 mm.

(minimizing the squared distance – least squares solution) the bent shape of the edge (Fig. S5c) and calculated the average curvature as $\kappa = 1/R$.

As for the volume inside the actuator’s cavity corresponding to each curvature measurement, it is important to note that we had to account for air compressibility. Since the syringe pump, the tubes and the actuator form a closed system, application of Boyle’s law yields,

$$p_0 v_0^{\text{sys}} = p v^{\text{sys}} \quad (\text{S1})$$

where p_0 is the initial pressure, p is the current pressure, v_0^{sys} is the total volume of the system at pressure p_0 and v^{sys} is the total volume of the system at pressure p . Note that the total initial volume of the system v_0^{sys} can be written as,

$$v_0^{\text{sys}} = v_0 + v_0^{\text{syringe}} + v_0^{\text{tube}} \quad (\text{S2})$$

where v_0 is the initial volume inside the actuator, v_0^{syringe} is the initial volume inside the syringe pump and v_0^{tube} is the initial volume inside the tubes used to connect the actuator

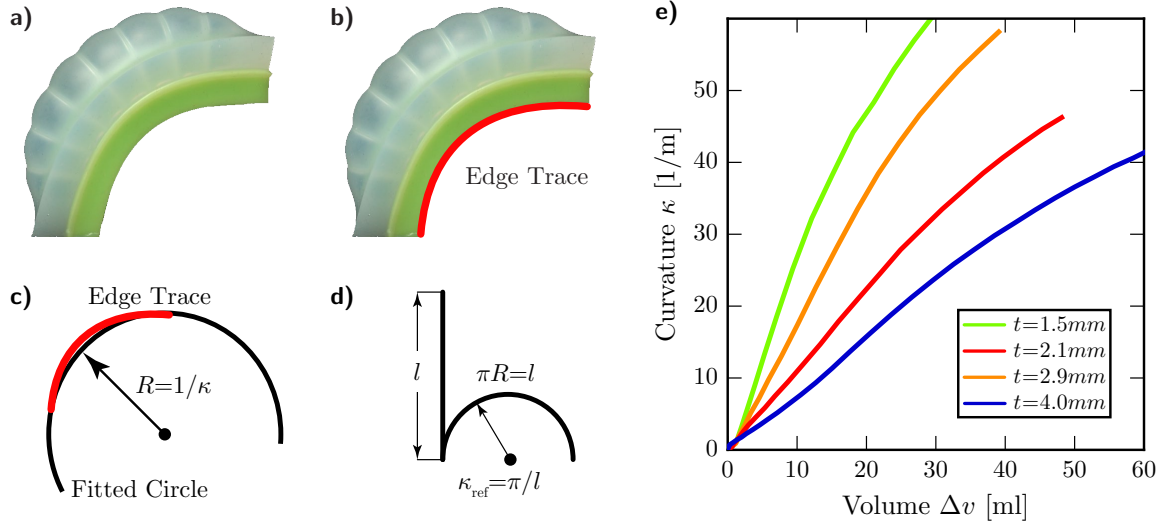


Figure S5: Determining the curvature of fluidic bending actuators upon inflation. (a) A snapshot of a bending actuator during inflation. (b) An image processing code identifies the bottom edge of the actuator, highlighted here in red. (c) The curvature of the actuator is calculated as the inverse radius of the circle that best fits the shape of the bottom edge. (d) To normalize the curvature measurements we use $\kappa_{\text{ref}} = \pi/l$, which is the curvature of a semi-circle with arc length equal to the initial length of the actuator's bottom edge (l). (e) Experimental curvature-volume curves for four actuators characterized by $t = 1.5, 2.1, 2.9$ and 4.0 mm.

to the syringe pump. Moreover, the total volume of the system v^{sys} at pressure p can be similarly expressed as,

$$v^{\text{sys}} = v_0^{\text{sys}} + \Delta v - \Delta v^{\text{syringe}} \quad (\text{S3})$$

where Δv is the change in volume inside the actuator and $\Delta v^{\text{syringe}}$ is the volume dispensed by the syringe pump. By combining equations Eq. S1, Eq. S2 and Eq. S3 and solving with respect to Δv we obtain,

$$\Delta v = \Delta v^{\text{syringe}} - \left(\frac{p - p_0}{p} \right) v_0^{\text{sys}} \quad (\text{S4})$$

which we use to determine the volume change in the actuator given the volume dispensed

by the syringe $\Delta v^{\text{syringe}}$ and the pressure p measured by the pressure sensor.

In Fig. S5e we report the evolution of the bending curvature κ as a function of the volume change inside the actuator, Δv , for all actuators tested in this study. The results show that the curvature increases almost linearly with the volume change and that actuators with larger top layer thickness need a larger Δv to achieve the same bending curvature, indicating that an increase in t leads to stiffer actuator.

Finite Element modeling

In an effort to better understand the effect of the actuator's thickness t on its response, we performed a series of Finite Element simulations. All numerical analyses were carried out using the commercial non-linear Finite Element software Abaqus (SIMULIA, Providence, RI). EcoFlex-30 was modeled as an incompressible Gent solid²³ (via a UHYPER user defined subroutine) with a shear modulus of $G = 19.43kPa$ and an extension limit of $J_m = 37.54$. Elite Double 32 was modeled as a nearly incompressible neo-Hookean solid²⁴ with shear modulus $G = 0.375MPa$ and Poisson's ratio $\nu = 0.4998$. All components of the actuator were meshed using 8-node fully integrated hybrid linear bricks (C3D8H) and perfect bonding was assumed between the two silicone rubbers. To determine the pressure-volume and curvature-volume relationships of each actuator, quasi-static non-linear simulations were performed using Abaqus/Standard. One end of the actuator was held completely fixed in space while the actuator was inflated using volume control through the fluid filled cavity interaction. While the pressure and volume inside the fluid cavity are both provided as post-processing variables, the curvature was determined by following the exact same procedure we used to post-process the experimental results.

To verify the validity of our numerical simulations, we first compared the numerical and experimental results for the pressure-volume and curvature-volume response of the

four tested actuators. The results shown in Fig. S6a and Fig. S6b compare the normalized pressure-volume and curvature-volume curves between FEA and experiments where pressure is normalized with the initial shear modulus of EcoFlex-30 ($G = 19.43kPa$), volume is normalized with the initial volume inside the actuator with top layer thickness $t = 4mm$ ($v_0^{\text{ref}} = 4078.125mm^3$) and curvature is normalized using $\kappa_{\text{ref}} = \pi/l = 41.88 \times 10^{-3}mm^{-1}$, which is the curvature of a semi-circle with arc length equal to the initial length of the actuator's bottom edge l (see Fig. S5d). The results indicate that the FEA simulations accurately capture the pressure-volume and curvature-volume responses of the fluidic bending actuators for all four considered values of t .

Having verified the accuracy of our numerical analyses, we next used our simulations to investigate the effect of t on both the pressure-volume and the curvature-volume responses. Specifically, we simulated the response of 22 actuators with different values of top layers thickness t ($t \in [1.5, 4.0]$ mm). The results shown in Figs. S6c and S6d indicate that for any given change in volume Δv , both the pressure and the curvature of the actuators vary almost linearly with t . As such, by linearly interpolating between these 22 curves, we built a response library from which we can determine the behavior of actuators with arbitrary top layer thickness within the range $t \in [1.5, 4.0]$ mm (Figs. S6e and S6f).

S2 Arrays of Interconnected Fluidic Actuators

In this section we first describe the setup we built to inflate an array of fluidic actuators connected via narrow tubes and then derive the governing equations that describe the response of such a system.

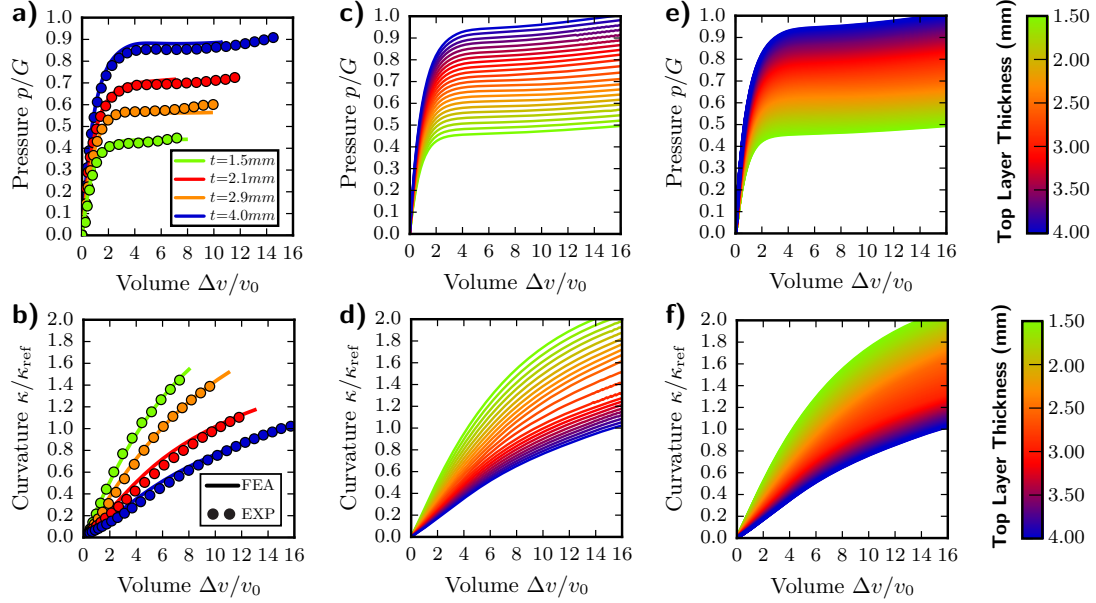


Figure S6: Finite Element simulations (a) Comparison between the experimental (markers) and numerical (continuous lines) pressure-volume curves for four actuators characterized by $t = 1.5, 2.1, 2.9$ and 4.0 mm. (b) Comparison between the experimental (markers) and numerical (continuous lines) curvature-volume curves for four actuators characterized by $t = 1.5, 2.1, 2.9$ and 4.0 mm. (c) Numerical pressure-volume curves for 22 actuators with $t \in [1.5, 4.0]$ mm. (d) Numerical curvature-volume curves for 22 actuators with $t \in [1.5, 4.0]$ mm. (e) Evolution of the pressure-volume response of the actuators as a function of t . (f) Evolution of the curvature-volume response of the actuators as a function of t .

Experimental Setup

The setup used to test our array of connected actuators is shown in Fig. S7a and consists of the actuators, narrow tubes to connect them, two pressure regulators, two solenoid valves, an LCD screen, a camera and an Arduino.

As shown in Fig. S7a, our system comprises four fluidic bending actuators connected to each other via narrow tubes (Extreme-Pressure PEEK Tubes -McMaster Carr 51085K41-51085K48). Specifically, we used tubes with an inner diameter of $0.005''$, $0.007''$, $0.01''$, $0.02''$ and $0.03''$ (depending on the experiment) and an outer diameter of $1/16''$. Note

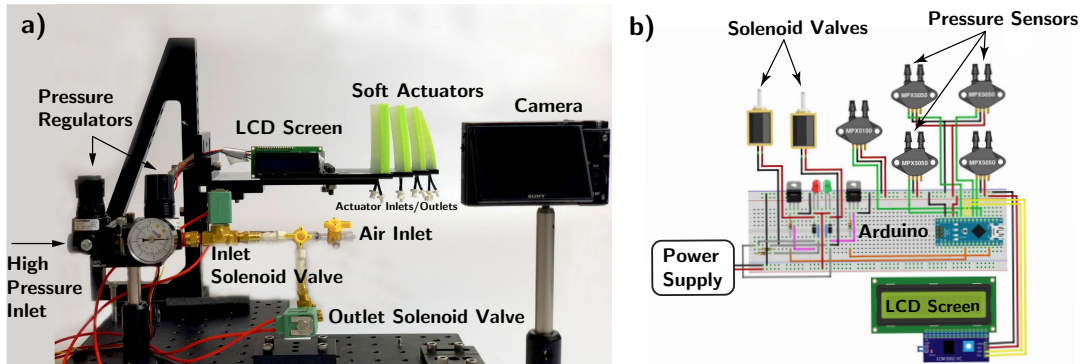


Figure S7: Experimental setup for testing arrays of interconnected fluidic actuators. (a) A photo of the setup highlighting the solenoid valves, the pressure regulators, the fluidic actuators, the LCD screen and the camera. (b) A schematic of the wiring for the Arduino with the solenoid valves, the pressure sensors and the LCD screen

that, since the tubes are rated for pressures up to 1000psi (6.98MPa), we expect the tube walls to not deform during our experiments and thus we consider them as rigid in our model (see Section *Modeling*).

To ensure a leak-free connection between the narrow tubes and the actuators, during fabrication we equipped all fluidic actuators with two PVC tubes with an inner diameter of 1/16" and outer diameter of 1/8" (McMaster Carr 9446K11) (see Fig. S8b). By choosing the inner diameter of the PVC tubes (1/16") to be the same as the outer diameter of the narrow tubes (1/16") we minimize the leaks occurring in the connections. Finally, we note that the last actuator in the sequence is only connected by a single tube (see Fig. S8a).

All narrow tubes except for the first connect two neighbouring actuators. As for the first tube, it connects the first actuator in the sequence to the pressure source (see Fig. S8a). In order to inflate the connected actuators at pressures in the order of a few kPa, we decreased the pressure from the wall air-outlet (~ 200 psi) using two pressure regulators (1/4 NPT 15CFM by Wilkerson and 1/4 NPT 9CFM by Coilhose Pneumatics) connected in series. The first pressure regulator reduces the inlet pressure from ~ 200

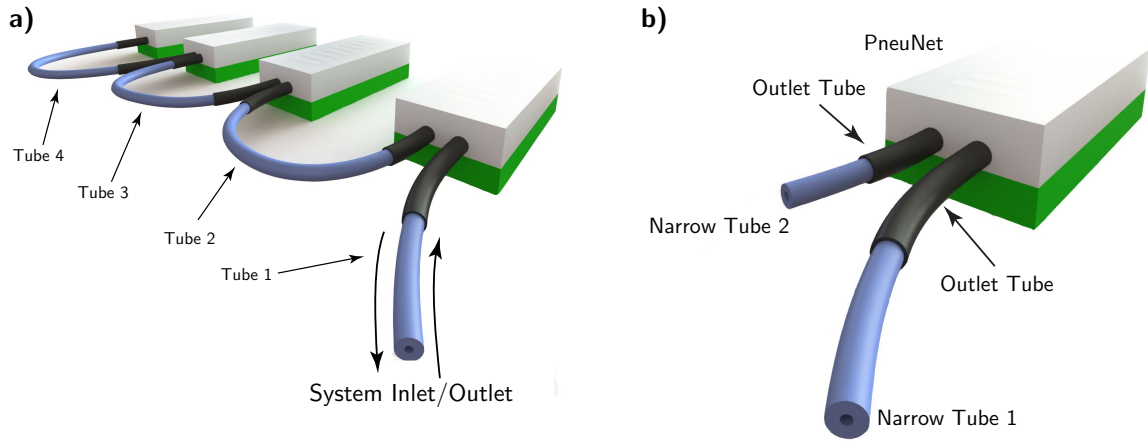


Figure S8: Array of interconnected fluidic actuators. (a) A 3D render of a system comprising 4 fluidic bending actuators interconnected via narrow tubes. The inlet of the first actuator serves as the inlet/outlet of the whole system. The last actuator in the array is only connected to a single narrow tube. (b) A 3D render of an individual fluidic bending actuator highlighting the inlet and outlet tubes. The narrow tubes are inserted into the outlet tubes which in turn are connected to the actuator

psi to about ~ 40 psi, while the second one accurately controls the pressure in the range $[0, 40]$ psi. Further, to turn on and off the input pressure we used two standard two-way solenoid valves (SC8256A002V - ASCO). One of the valves was used to switch on/off the input pressure, while the second one was used to switch on/off the outlet of the system to the atmosphere, so that the actuators could deflate and return to their initial state (i.e. when the input solenoid was open, the outlet solenoid was closed and vice-versa). Both solenoid valves were powered through an external power supply using $\sim 9V$ and $\sim 0.1A$ and controlled via an NPN transistor (IRF520 - Vishay Siliconix).

To monitor and record both the input pressure and the pressure inside each actuator we equipped the setup with 5 pressure sensors all connected to the Arduino. To measure the input pressure we used a sensor rated for use up to ~ 400 kPa (MPX5100DP-ND - NXP USA Inc.), while to measure the pressure inside the actuators we used sensors rated for use up to ~ 200 kPa (MPX5050DP-ND - NXP USA Inc.).

Finally, to capture the deformation experienced by the actuators upon pressurization we used a digital camera (Sony RX100 IV). Note that we used the LCD screen, which displayed whether the input pressure was on or off, to sync the recorded videos with the pressure readings.

Modeling

The system considered in this study comprises several fluidic bending actuators connected via narrow tubes. To capture its response we not only need to be able to capture the behavior of the actuators, but also to determine the amount of fluid exchanged through the tubes. To this end, we focus on the $[i]$ -th tube in the system, which has length L_i , circular cross section with radius R_i (with $L_i \gg R_i$) and is connected to actuators $[i - 1]$ and $[i]$, as shown in Fig. S9a. We further introduce an orthonormal local direction basis, where \mathbf{e}_z is identified as the unit vector along the tube's length and \mathbf{e}_r and \mathbf{e}_θ lie in the plane of the cross-section (see Fig. S9a). To determine the amount of fluid exchanged through the tube up to time t , $\tilde{v}_i(t)$, we assume that

- (i) the tube walls are rigid and not deformed by the flow. Note that this assumption is motivated by the fact that the tubes used in our experiments are rated for much higher pressures ($\sim 10^3$ psi) than the ones developed in our actuators (~ 3 psi).
- (ii) the head losses due to friction at the connections between the tubes and the actuators can be captured by the equivalent length method, adjusting the tube's length to $L_{i,eq}$.^{S1}
- (iii) the radial (u_r) and angular (u_θ) components of the fluid velocity field \mathbf{u} are zero (since $L_i \gg R_i$), so that

$$\mathbf{u}(r, \theta, z, t) = u_z(r, z, t)\mathbf{e}_z, \quad (\text{S5})$$

where we also dropped the dependency on θ because of cylindrical symmetry.

(iv) the flow is incompressible, so that

$$\nabla \cdot \mathbf{u} = 0 \Rightarrow \frac{\partial u_r}{\partial r} + \frac{1}{r} \frac{\partial u_\theta}{\partial \theta} + \frac{\partial u_z}{\partial z} = 0 \Rightarrow \frac{\partial u_z}{\partial z} = 0, \quad (\text{S6})$$

indicating that u_z does not depend on z (i.e. $u_z(r, t)$)

(v) the fluid flow is laminar and governed by the Navier–Stokes equations, which in light of Eqs. S5 and S6 reduces to ²

$$\frac{\partial u_z}{\partial t} = -\frac{1}{\rho} \frac{\partial p}{\partial z} + \frac{\mu}{r} \frac{\partial}{\partial r} \left(r \frac{\partial u_z}{\partial r} \right), \quad (\text{S8})$$

where ρ is the fluid density, μ is the dynamic viscosity of the fluid and p is the pressure in the tube.

(vi) the fluid velocity profile has the form,

$$u_z(r, t) = F_i(t) \left[\left(\frac{r}{R_i} \right)^2 - 1 \right], \quad (\text{S9})$$

where $F_i(t)$ is an unknown function that, since the volumetric flow rate through the $[i]$ -th tube ($d\tilde{v}_i(t)/dt$) is given by

$$\frac{d\tilde{v}_i(t)}{dt} = \int_0^{R_i} u_z(r, t) 2\pi r dr = -\frac{1}{2} \pi R_i^2 F_i(t), \quad (\text{S10})$$

²Note that a closed-form analytical solution to Eq. S8 exists for steady state conditions and is given by^{S2},

$$u_z(r) = \frac{\Delta p R_i^2}{4\mu L_i} \left[\left(\frac{r}{R_i} \right)^2 - 1 \right], \quad (\text{S7})$$

where Δp is the (constant) difference in pressure between the two ends of the tube. However, this solution is unable to capture the response of our system, since Δp is determined by the pressure inside the two actuators connected to the tube and continuously changes with time as the fluid flows. The velocity field proposed in Eq. S9 does not satisfy the Navier–Stokes equations in a point-wise manner, but meets the no-slip boundary conditions at the tube walls and provides a very good approximation for the volumetric flow, which is the main interest of this study. Analytical solutions to Eq. S8 under transient conditions only exist for the starting flow in a tube with a constant pressure gradient and are very complicated.^{S3} The highly non-linear and time-varying pressure gradient experienced by the fluid in our system prohibits analytical solutions to Eq. S8

can be expressed as

$$F_i(t) = -\frac{2}{\pi R_i^2} \frac{d\tilde{v}_i(t)}{dt}. \quad (\text{S11})$$

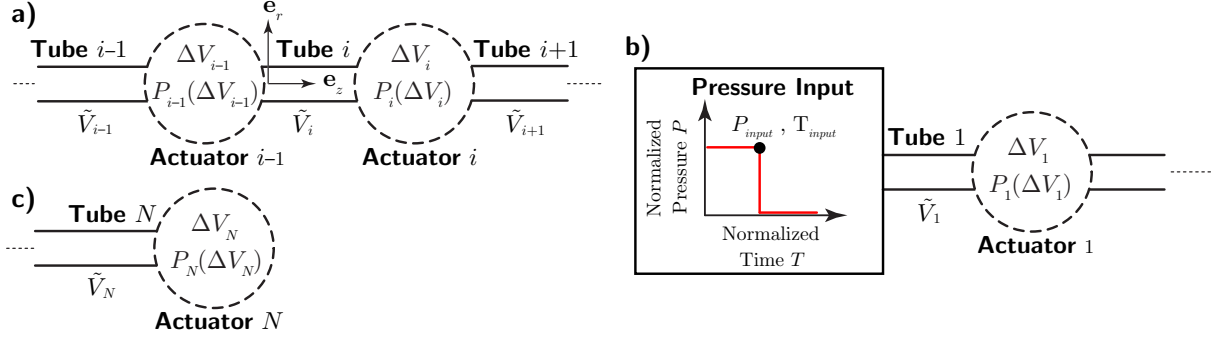


Figure S9: Array of interconnected fluidic actuators. (a) A schematic of the system. Note that the $[i]$ -th tube is connected to the $[i - 1]$ -th and $[i]$ -th actuators. (b) A schematic of the first tube in the array, which has the left end connected to the pressure source and the right one connected to the $[1]$ -st actuator in the array. (c) A schematic of the last tube in the array, which is connected to the $[N - 1]$ -th and $[N]$ -th actuators

Next, we substitute Eqs. S9 and S11 into Eq. S8 and integrate along the volume of the tube to obtain,

$$L_{i,eq} \frac{d^2 \tilde{v}_i(t)}{dt^2} = -\frac{\pi R_i^2}{\rho} (p_i - p_{i-1}) - \frac{8\mu L_{i,eq}}{R_i^2} \frac{d\tilde{v}_i(t)}{dt}, \quad (\text{S12})$$

where p_i is the pressure inside the $[i]$ -th actuator. Upon the introduction of the normalized volumetric flow $\tilde{V}_i = \tilde{v}_i/v_0$ (v_0 denoting the volume of the smallest actuator in the system), time $T = t/t_{max}$ (t_{max} denoting the response time of the system) and pressure $P_i = p_i/G$ (with G being the shear modulus of the material used to fabricate the actuators), Eq. (S12) can be rewritten in dimensionless form as

$$\varepsilon_i \frac{d^2 \tilde{V}_i(T)}{dT^2} + \frac{d\tilde{V}_i(T)}{dT} + \xi_i (P_i - P_{i-1}) = 0, \quad (\text{S13})$$

with

$$\varepsilon_i = \frac{R_i^2 \rho}{8\mu t_{max}}, \quad \text{and} \quad \xi_i = \frac{\pi G R_i^4 t_{max}}{8\mu L_{i,eq} v_0}. \quad (\text{S14})$$

It is important to point out that for narrow tubes with $L_{i,eq} \gg R_i$, as those considered in this study, the product $\varepsilon_i \xi_i$ is typically very small ($\varepsilon_i \xi_i \ll 1$). Using the representative values presented in Table S2 we find that for air $\varepsilon_{\text{air}} = 5.1 \times 10^{-6}$ and $\xi_{\text{air}} = 268.27$ and for water $\varepsilon_{\text{water}} = 7.25 \times 10^{-5}$ and $\xi_{\text{water}} = 4.92$, resulting in $\varepsilon_{\text{air}} \xi_{\text{air}} = 0.001368$ and $\varepsilon_{\text{water}} \xi_{\text{water}} = 0.00035$. Consequently, for the tubes in our systems, in which viscous forces dominate inertia, Eq. S13 can be simplified to (see Section “On the Simplification of Equation S13”).

$$\frac{d\tilde{V}_i(T)}{dT} + \xi_i (P_i - P_{i-1}) = 0. \quad (\text{S15})$$

Eq. S15, which describes the volumetric flow in a narrow tube connected to fluidic actuators, is frequently considered the Ohm’s law analog for electrical circuits.^{S4} In this context, $1/\xi_i$ expresses the equivalent resistance that the tube imposes to fluid flow; when ξ_i is large, high flow rates dV_i/dT are achieved for relatively low pressure differences, whereas when ξ_i is small, the opposite is true. Finally, since the normalized change in volume for the $[i]$ -th actuator, $\Delta V_i = \Delta v_i/v_0$, can be expressed in terms of the volumetric flows exchanged through the two tubes connected to it as

$$\Delta V_i = \tilde{V}_i - \tilde{V}_{i+1}, \quad (\text{S16})$$

Eq. (S15) can be rewritten as

$$\frac{d\Delta V_i(T)}{dT} + \xi_i (P_i - P_{i-1}) - \xi_{i+1} (P_{i+1} - P_i) = 0. \quad (\text{S17})$$

For a system comprising N fluidic actuators interconnected via narrow tubes Eq. S17 result in a system of N coupled differential equations, which given a pressure-volume relationship for the actuators that can be numerically solved to determine the normalized change in volume for the $[i]$ -th actuator as a function of time. Once the volume history for all actuators is known, their bending curvature is then determined using the corresponding

curvature-volume relationship. Finally, we note that for the first and last tube in the array Eq. S17 needs to be modified to

$$\frac{d\Delta V_1(T)}{dT} + \xi_1 (P_1 - P_{input}(T)) - \xi_2 (P_2 - P_1) = 0, \quad (\text{S18})$$

$$\frac{d\Delta V_N(T)}{dT} + \xi_N (P_N - P_{N-1}) = 0, \quad (\text{S19})$$

to account for the pressure input (see Fig. S9b) and the end of the array (see Fig. S9c).

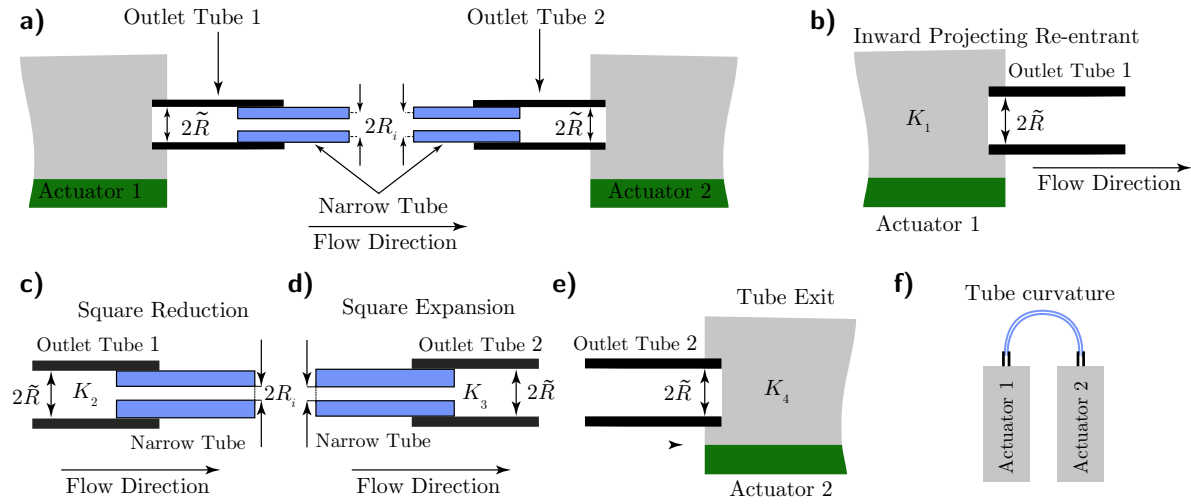


Figure S10: Minor Losses in the tubes. (a) Schematic of the tube connections between two actuators, highlighting the sudden radii transitions from one tube to another. (b) Schematic of the inward projecting re-entrant transition associated with K_1 (b) Schematic of the square reduction transition associated with K_2 . (c) Schematic of the square-expansion transition associated with K_3 . (d) Schematic of the tube exit transition, associated with K_4 . (e) Schematic of the tube curvature associated with K_5

As for the adjusted length $L_{i,eq}$, according to the equivalent length method^{S1} it can be written as

$$L_{i,eq} = L_i + \frac{R_i}{f_{i,D}} \sum_{\alpha}^{N_{i,t}} K_{i,\alpha}, \quad (\text{S20})$$

where $N_{i,t}$ are the number of minor losses associated with the $[i]$ -th tube and $f_{i,D}$ is the Darcy friction factor, which for laminar flow is defined as^{S2}

$$f_{i,D} = \frac{64}{Re_i}, \quad (\text{S21})$$

$Re_i = (2 \rho v_0)/(\mu \pi R_i t_{max})dV_i/dT$ being the Reynolds number for the $[i]$ -th tube. Moreover, $K_{i,\alpha}$ is referred to as the K-value for the α -th minor loss in the tube and is either read from tables or has particular formulas depending on the type of geometric transitions in the tube. Specifically, for all tubes in our system we have $N_{i,t} = 5$ (see Fig. S10) and

- ($\alpha=1$) minor loss associated with the transition from the actuator chamber to the PVC outlet tube inserted into the actuator (see Fig. S10b), for which^{S1}

$$K_{i,1} = 0.78, \quad \forall i = 1, \dots, N \quad (\text{S22})$$

- ($\alpha=2$) minor loss associated with the transition from the outlet PVC tube with radius \tilde{R} inserted into the actuator to the narrow tube with radius R_i (see Fig. S10c), for which^{S1}

$$K_{i,2} = \left[1.2 + \frac{160}{Re} \right] \left[\left(\frac{\tilde{R}}{R_i} \right)^4 - 1 \right], \quad \forall i = 1, \dots, N \quad (\text{S23})$$

- ($\alpha=3$) minor loss associated with the transition from the narrow tube with radius R_i to the outlet tube with radius \tilde{R} inserted into the actuator (see Fig. S10c), for which^{S1}

$$K_{i,3} = 2 \left[1 - \left(\frac{R_i}{\tilde{R}} \right)^4 \right], \quad \forall i = 1, \dots, N \quad (\text{S24})$$

- ($\alpha=4$) minor loss associated with the transition from the outlet tube inserted into the actuator to the actuator chamber (see Fig. S10e), for which^{S1}

$$K_{i,4} = 1.0, \quad \forall i = 1, \dots, N \quad (\text{S25})$$

- ($\alpha=5$) minor loss due to the curvature of each tube for which^{S1}

$$K_{i,5} = 1.5, \quad \forall i = 1, \dots, N \quad (\text{S26})$$

Table S2: Representative parameter values for this study

Parameter	Value
Tube Radius, R	0.381 mm
Tube Length, L	20 cm
Stiffness, G	19.43 kPa
Initial Actuator Volume, v_0	4078.125 mm ³
System Response Time, t_{max}	25 sec

In this study we consider systems comprising either 2 or 4 interconnected bending fluidic actuators (i.e. $N = 2$ or 4), so that Eq. S17 becomes a system of either 2 or 4 coupled ODEs. To determine the pressure P_i inside the $[i]$ -th actuator (characterized by the geometric parameter t_i) for a given change in volume ΔV_i , we use the numerically determined pressure volume response library shown in Fig. S6e. For the pressure input supplied to the system, we consider a rectangular pulse (see Fig. S9b)

$$P_{input}(T) = \begin{cases} P_{input}, & \text{for } T \leq T_{input} \\ 0, & \text{for } T > T_{input} \end{cases} \quad (\text{S27})$$

Furthermore, we consider $\mu = 1.568 \times 10^{-5} Pa \cdot s$ (corresponding to the dynamic viscosity of air at room temperature), $t_{max} = 25$ sec, $v_0 = 4078.125$ mm³ (corresponding to the volume of a bending actuator with $t = 4$ mm) and $G = 19.43$ kPa (corresponding to the shear modulus of EcoFlex-30), yielding

$$\xi_i = 2.98309 \times 10^{15} \times \frac{R_i^4}{L_{i,eq}} \quad (\text{S28})$$

Finally, to integrate Eq. S17 we use a Python implementation of the Real-valued Variable-coefficient Ordinary Differential Equation solver, (LSODA) with initial conditions

$$\Delta V_i(0) = 0 \quad \forall i = 1, \dots, N. \quad (\text{S29})$$

Equivalence between Eqs. S13 and S15 in systems for which $\varepsilon\xi \ll 1$

In this Section we demonstrate that in systems for which the product $\varepsilon\xi$ is very small Eq. S15 (i.e. the simplified form of the governing equation) is identical to Eq. S13 (i.e. the governing equation). To this end, we first quantify the product $r = \varepsilon\xi$ in our system comprised of narrow and slender tubes in which viscous forces dominate

$$\begin{aligned}
 r = \varepsilon\xi &= \frac{R^2 \rho}{8\mu t_{max}} \frac{\pi GR^4 t_{max}}{8\mu L v_0} = \\
 &= \left(\frac{1}{64\pi} \right) \underbrace{\left(\frac{G(\pi R^2)}{(\mu^2/\rho)} \right)}_{r_F} \underbrace{\left(\frac{\pi R^2 L}{v_0} \right)}_{r_V} \underbrace{\left(\frac{R}{L} \right)^2}_{r_a^2} = \\
 &= \left(\frac{1}{64\pi} \right) r_F r_V r_a^2 \ll 1
 \end{aligned} \tag{S30}$$

where,

- r_F is the ratio between the force associated with the pressure gradient ($G\pi R^2$) and the viscous forces in the tube (μ^2/ρ)
- r_V is the ratio between the volume inside the tubes ($L\pi R^2$) and the volume inside the actuators (v_0)
- r_a is the aspect ratio of the tube defined as the radius (R) divided by the length (L)

Since in our system r_F , r_V and r_a are always individually very small numbers, Eq. S30 indicates that $\varepsilon\xi \ll 1$.

Next, to explain the validity of Eq. S13 when $\varepsilon\xi \ll 1$, we study the analytical solution of a very simple system consisting of a single narrow tube connected to a single pneumatic actuator and a pressure source (see Fig. S11), for which Eq. S13 reduces to

$$\varepsilon \frac{d^2 \tilde{V}}{dT^2} + \frac{d\tilde{V}}{dT} + \xi(P - P_{input}) = 0. \tag{S31}$$

Assuming that (i) the input provides a constant pressure, $P_{input} = 1$; (ii) the actuator has a linear pressure-volume response, $P(\Delta V) = \Delta V$; and (iii) the initial conditions are $\tilde{V}(0) = 0$, $\tilde{V}'(0) = -\xi$, Eq. S31 admits the analytical solution in the form

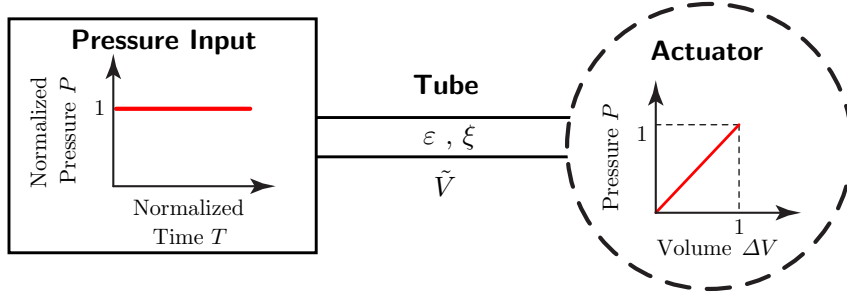


Figure S11: A simple system consisting of a single narrow tube, a single fluidic actuator and a pressure source supplying a constant pressure

$$\begin{aligned} \tilde{V}(T) = & 1 + A(\varepsilon, \xi) \exp \left[-\frac{T}{2\varepsilon} \left(1 + \sqrt{1 - 4\varepsilon\xi} \right) \right] \\ & - B(\varepsilon, \xi) \exp \left[-\frac{T}{2\varepsilon} \left(1 - \sqrt{1 - 4\varepsilon\xi} \right) \right], \end{aligned} \quad (\text{S32})$$

where

$$A(\varepsilon, \xi) = \frac{1 - 2\varepsilon\xi - \sqrt{1 - 4\varepsilon\xi}}{2\sqrt{1 - 4\varepsilon\xi}}, \quad (\text{S33})$$

$$B(\varepsilon, \xi) = \frac{1 - 2\varepsilon\xi + \sqrt{1 - 4\varepsilon\xi}}{2\sqrt{1 - 4\varepsilon\xi}}. \quad (\text{S34})$$

By substituting $\varepsilon = r/\xi$, Eqs. S32-S34 can be rewritten as

$$\begin{aligned} \tilde{V}(T) = & 1 + A(r) \exp \left[-\frac{\xi T}{2r} \left(1 + \sqrt{1 - 4r} \right) \right] \\ & - B(r) \exp \left[-\frac{\xi T}{2r} \left(1 - \sqrt{1 - 4r} \right) \right], \end{aligned} \quad (\text{S35})$$

with

$$A(r) = \frac{1 - 2r - \sqrt{1 - 4r}}{2\sqrt{1 - 4r}}, \quad (\text{S36})$$

$$B(r) = \frac{1 - 2r + \sqrt{1 - 4r}}{2\sqrt{1 - 4r}}, \quad (\text{S37})$$

which for $r \ll 1$ can then be expressed using Taylor expansion as

$$\tilde{V}(T) = 1 - \exp(-T\xi) + \mathcal{O}(r^2). \quad (\text{S38})$$

Having determined the analytical solution of Eq. S31, we now focus on the simplified governing equation,

$$\frac{d\tilde{V}}{dT} + \xi(P - P_{input}) = 0. \quad (\text{S39})$$

Importantly, we find that for the same system and boundary conditions Eq. S39 admits the analytical solution

$$\tilde{V}(T) = 1 - \exp(-T\xi), \quad (\text{S40})$$

which is identical to Eq. S38 up to second order terms with respect to r . Therefore, the analysis of the simple system justifies the simplification of the governing equation used in this study.

Non-Dimensional Extents within which the Model Assumptions are Valid

Our numerical model, just like all models, is fundamentally based on the assumptions stated in the Forward Modeling Section of the Main text (also in the Modeling Section of the SI). If any of the assumptions is violated the model is not expected to maintain its

predictive capabilities. In the following we will address each of the assumptions on which the model is based on and quantify the relevant non-dimensional extents within which each assumption is valid.

- i) The tube walls are rigid and not deformed by the flow.

To assess the validity of this approximation one should analytically estimate the expected change in the radius of the tube due to the internal pressure. To this end, we assume that the maximum pressure developed due to the flow is equal to p_{max} and that the tube has thickness t , radius R and is made of a material with Young's modulus E and Poisson's ratio ν . Furthermore, we approximate the tube as a thick-walled linearly elastic pressure vessel, so that the stresses at the inner surface of the tube are given by,

$$\sigma_{rr} = -p_{max}, \quad (\text{S41})$$

$$\sigma_{\theta\theta} = p_{max} \frac{(R+t)^2 + R^2}{(R+t)^2 - R^2}, \quad (\text{S42})$$

$$\sigma_{zz} = p_{max} \frac{R^2}{(R+t)^2 - R^2}. \quad (\text{S43})$$

It follows from Eqs. S41–S43 that the circumferential strain can be expressed as

$$\varepsilon_{\theta\theta} = \frac{1}{E} [\sigma_{\theta\theta} - \nu(\sigma_{rr} + \sigma_{zz})] = \left(\frac{p_{max}}{E} \right) \frac{(2 - \nu)R^2 + 2(\nu + 1)Rt + (\nu + 1)t^2}{t(2R + t)}, \quad (\text{S44})$$

At this point is it important to point out that the rigid tube-walls assumption is valid if $\varepsilon_{\theta\theta} \ll 10^{-3} = 0.1\%$. Since in this study we used tubes characterized

by $E \simeq 3.8\text{GPa}$, $\nu \simeq 0.38$ $R = 0.381\text{mm}$, and $t = 0.4064\text{mm}$ and the maximum pressure in the tubes (due to the input pressure) was $p_{max} = 100\text{kPa}$, we find through Eq. (S44) that $\varepsilon_{\theta\theta} = 4.9 \cdot 10^{-5}$, justifying the validity of the rigid wall assumption made in our study.

ii) The head losses due to friction at the connections between the tubes and the actuators can be captured by the equivalent length method, adjusting the tube's length to L_{eq} .

As long as such connections exist in the system, this approximation will always be valid provided that the flow is laminar, incompressible and inviscid effects are negligible.

iii) The radial (u_r) and angular (u_θ) components of the fluid velocity field \mathbf{u} are zero (since $L \ll R$), so that

$$\mathbf{u}(r, \theta, z, t) = u_z(r, z, t)\mathbf{e}_z.$$

This assumption relies on the fact that the length of the tube is much larger than its radius $L \gg R$ and is valid if

$$\frac{L}{R} \gg 10.$$

iv) The flow is incompressible.

To assess the validity of this assumption we start from the continuity condition which states,

$$\frac{D\rho}{Dt} = 0 \Rightarrow \frac{\partial\rho}{\partial t} + \nabla \cdot (\rho\mathbf{u}) = 0 \Rightarrow \frac{\partial\rho}{\partial t} = -\rho\nabla \cdot \mathbf{u} - \mathbf{u} \cdot \nabla\rho \quad (\text{S45})$$

The density gradient $\nabla\rho$ can be expressed in terms of the pressure gradient ∇p by making use of the chain rule to find

$$\nabla p = \underbrace{\frac{dp}{d\rho}}_{c^2} \nabla\rho \Rightarrow \nabla p = c^2 \nabla\rho \Rightarrow \nabla\rho = \frac{1}{c^2} \nabla p \quad (\text{S46})$$

where $c = \sqrt{dp/d\rho}$ is the local speed of sound. Therefore, by combining Eq. S45 and Eq. S46 we find

$$\frac{\partial\rho}{\partial t} = -\rho\nabla \cdot \mathbf{u} - \frac{\mathbf{u}}{c^2} \nabla p \quad (\text{S47})$$

For the flow to be incompressible, the term $\partial\rho/\partial t$ needs to vanish implying that the density of the fluid does not vary as a result from the flow. To this end, the incompressibility assumption is valid if,

$$\nabla \cdot \mathbf{u} = 0 \quad \text{and} \quad \frac{\mathbf{u}}{c^2} \nabla p = 0 \quad (\text{S48})$$

Given that the radial and angular velocity components vanish $u_r = u_\theta = 0$ (following from a prior assumption) the first requirement for incompressibility suggests that,

$$\nabla \cdot \mathbf{u} = \frac{\partial u_r}{\partial r} + \frac{1}{r} \frac{\partial u_\theta}{\partial \theta} + \frac{\partial u_z}{\partial z} = 0 \Rightarrow \frac{\partial u_z}{\partial z} = 0 \quad (\text{S49})$$

which is valid for long and narrow tubes for which,

$$\frac{L}{R} \gg 10 \quad (\text{S50})$$

The second requirement for incompressible flow is immediately satisfied in the case where the velocity magnitude of the flow is much smaller than the speed of sound since,

$$\left| \frac{\mathbf{u}}{c} \right| \ll 1 \Rightarrow \frac{\mathbf{u}}{c^2} \nabla p = 0 \quad (\text{S51})$$

v) The flow is laminar and governed by the Navier Stokes equations which reduce to

$$\frac{\partial u_z}{\partial t} = -\frac{1}{\rho} \frac{\partial p}{\partial z} + \frac{\mu}{r} \frac{\partial}{\partial r} \left(r \frac{\partial u_z}{\partial r} \right)$$

To assess the validity of this assumption we have to estimate the Reynolds number for the system

$$Re = \frac{u \rho R}{\mu} = \frac{\frac{dv}{dt} \rho R}{\pi R^2 \mu} = \frac{dv}{dt} \frac{\rho}{\pi R \mu},$$

If Re is found to be less than 2500 then the assumption holds; otherwise the flow is not expected to be fully laminar. To this end, we express the non-dimensional flow rate $d\tilde{V}/dT$ in terms of the Reynolds number as,

$$\frac{d\tilde{V}}{dT} = \frac{dv}{dt} \frac{t_{max}}{v_0} = Re \frac{\pi t_{max} R \mu}{\rho v_0}$$

According to Eq. S15, the governing equation for a system comprising a single actuator connected to the input source via a single narrow tube,

$$\frac{d\tilde{V}}{dT} + \xi\Delta P = 0$$

For such a system, the maximum Reynolds number is expected at $T = 0$ where the pressure gradient is maximum. At $T = 0$ we have $\Delta P = -P_{input}$ and thus,

$$\max \left| \frac{d\tilde{V}}{dT} \right| = \xi P_{input} \quad (\text{S52})$$

Therefore, the maximum expected Reynolds number in this case is given by,

$$Re_{max} = \frac{\xi \rho P_{input} v_0}{\pi t_{max} R \mu}$$

Substituting representative values for our study (see Table S2) we find that $Re_{max} \approx 2400$. As a result, since the maximum expected Reynolds number is less than 2500 the flow is expected to be laminar justifying this assumption.

(vi) The fluid velocity profile has the form

$$u_z(r, t) = F_i(t) \left[\left(\frac{r}{R_i} \right)^2 - 1 \right], \quad (\text{S53})$$

where $F_i(t)$ is an unknown function.

This assumption is motivated by the Poiseuille flow since the spatial component of the velocity profile is chosen so that it satisfies the no-slip boundary conditions at the tube walls. The temporal component of the velocity field is an unknown function of time to be determined. This assumption is expected to

be valid in all scenarios where the flow satisfies the no-slip boundary condition. However, as noted in the Section "Modeling" of the Supporting Information it doesn't satisfy the Navier-Stokes equations in a point-wise manner, but still provides a very good approximation for the volumetric flow which is the main interest of this study.

Inverse Design & Optimization

Numerical solutions of Eq. S17 can be used to predict the temporal response of arbitrary arrays of fluidic actuators connected via narrow tubes. Here we are interested in the inverse problem of designing a system capable of achieving a target response. Specifically, we want the $[i]$ -th actuator in the array to attain a specified maximum bending curvature $K_{i,max} = \kappa_{i,max}/\kappa_{ref}$ at a predefined time $T_{i,max} = t_{i,max}/t_{max}$ and then to completely deflate. Since in this study we only consider systems consisting of 4 narrow tubes and 4 fluidic bending actuators with different top layer thickness t and use a rectangular pulse as input pressure, the parameters that need to be determined to achieve such a target response are

- the parameter t_i defining the geometry of each actuator in the array (with $i = 1, 2, 3, 4$);
- the radius to length ratio of the tubes defined by the dimensionless parameter ξ_i (with $i = 1, 2, 3, 4$);
- the magnitude of the input pressure P_{input} and the pressurization time T_{input} .

To find the set of parameters resulting in the desired response, we then minimize

$$\mathcal{Z} = \sum_{i=1}^4 (d_i + w \tau_i) \quad (\text{S54})$$

where d_i is the “distance” in the $K - T$ space between the target and actual points of maximum curvature for the $[i]$ -th bending actuator,

$$d_i = \sqrt{\Delta K_i^2 + \Delta T_i^2}, \quad (\text{S55})$$

with

$$\Delta K_i = K_{i,max} - \max_T K_i(T), \quad (\text{S56})$$

$$\Delta T_i = T_{i,max} - \operatorname{argmax}_T K_i(T). \quad (\text{S57})$$

Moreover, τ_i denotes the amount of time that the $[i]$ -th actuator spends above a threshold curvature $\kappa_{thres}^{(i)} = 0.05\kappa_{max}^{(i)}$ and is introduced to ensure that all actuators quickly deflate (i.e. reach $\kappa = 0$) after reaching the target point of maximum curvature. Finally, the factor w is a weight that sets the relative importance of the two objectives; $w \rightarrow 0$ expresses a bias towards solutions that just minimize $d^{(i)}$, while very large w results in solutions that minimize only $\tau^{(i)}$. By trial and error, we found that for our system $w = 1/4$ leads to the best results.

Finally, we input all of this information together with the models we developed in the previous section (Eq. S17) and the actuators’ response (see Figs. S6e and f) into a Python implementation of the Covariance Matrix Adaptation Evolution Strategy^{S5} (CMA-ES). CMA-ES is an evolutionary algorithm that is used to solve optimization/inverse problems by iteratively solving several forward problems to adjust a covariance matrix of the solution. CMA-ES is a derivative free algorithm, well suited for optimization problems of high dimensionality. Even though CMA-ES is not as fast as gradient-based algorithms, in our study it outperformed the latter since the objective function defined by Eqs. S54–S56 is non-differentiable. To ensure that all the parameters involved in the optimization have

similar orders of magnitude, we renormalize them to lie in the interval $[0, 1]$. To this end, we define the renormalized tube resistances $\hat{\xi}_i$, actuators top layer thicknesses \hat{t}_i , input pressure \hat{P}_{input} and pressurization time \hat{T}_{input} as

$$\hat{\xi}_i = \frac{\xi_i - \xi_{min}}{\xi_{max} - \xi_{min}} \quad (\text{S58})$$

$$\hat{t}_i = \frac{t_i - t_{min}}{t_{max} - t_{min}} \quad (\text{S59})$$

$$\hat{P}_{input} = \frac{P_{input} - P_{input_{min}}}{P_{input_{max}} - P_{input_{min}}} \quad (\text{S60})$$

$$\hat{T}_{input} = \frac{T_{input} - T_{input_{min}}}{T_{input_{max}} - T_{input_{min}}} \quad (\text{S61})$$

where $\xi_{max} = 62863$, $\xi_{min} = 31.4$, $t_{max} = 4.0$ mm, $t_{min} = 1.5$ mm, $P_{input_{max}} = 25$, $P_{input_{min}} = 0$, $T_{input_{max}} = 0.25$ and $T_{input_{min}} = 0$. The initial values for all variables used at the beginning of the optimization are drawn from a standard normal distribution. Apart from the initial values of all the variables, CMA-ES also requires the initial standard deviation to generate new candidate solutions in the first generation of solutions. After trial and error, we found that an initial standard deviation of $\sigma = 0.4$ was a reasonable choice to ensure a “rich in variety” first generation of solutions given that all variables lie in the interval $[0, 1]$. Note that the parameter bounds are enforced using rejection and resampling. Whenever CMA-ES generates new parameter values that lie outside the $[0, 1]$ interval, the values are rejected and new ones are generated until all candidate parameter values are within the $[0, 1]$ interval.

Results

In this study we consider systems comprising four bending actuators connected via four narrow tubes, choose the system response time to be $t_{max} = 25$ secs and use tubes with

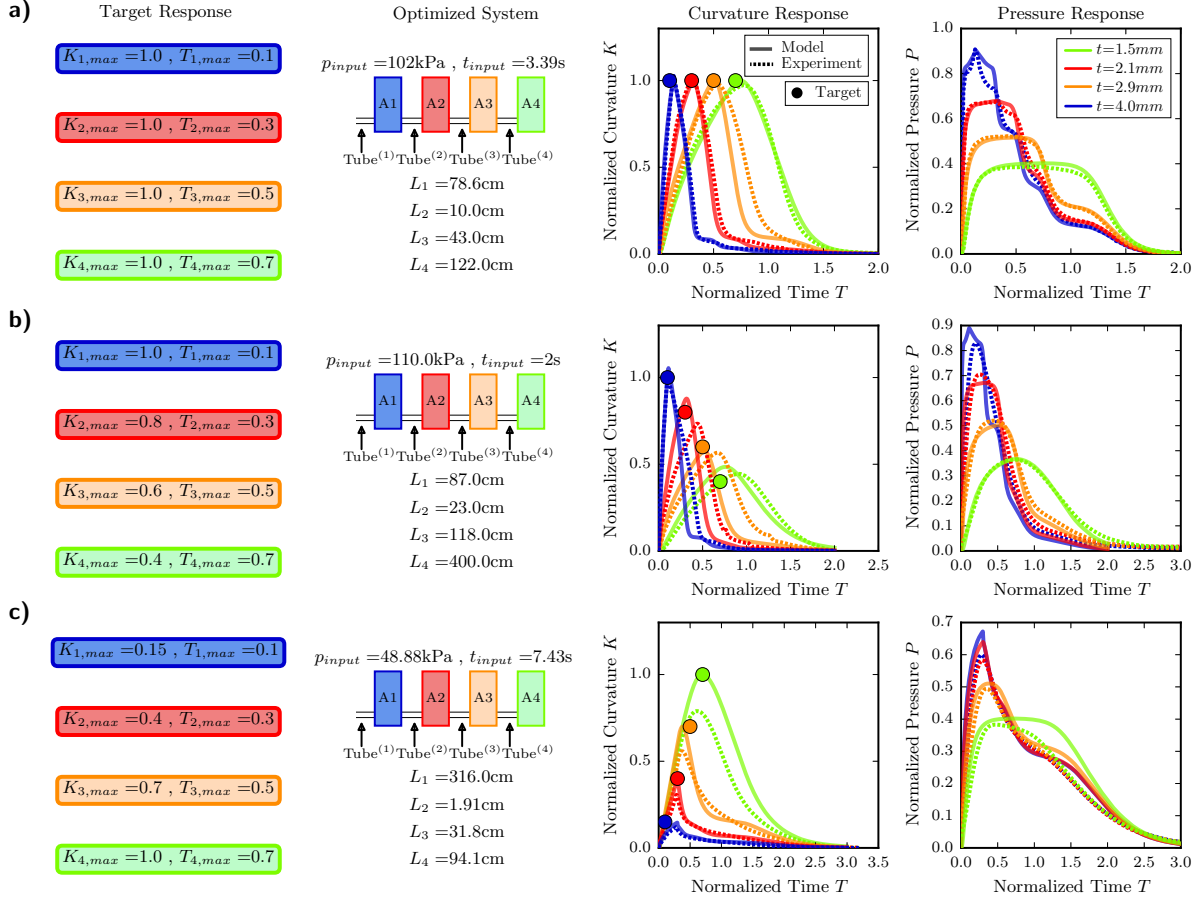


Figure S12: Optimal solutions to the inverse problem for a system comprising four bending actuators connected via four narrow tubes. The top layer thickness of the actuators are fixed to be $t_1 = 4.0$ mm, $t_2 = 2.9$ mm, $t_3 = 2.1$ mm and $t_4 = 1.5$ mm. The system response time is chosen as $t_{max} = 25$ sec and the tube radii are fixed to $R = 0.38$ mm. The optimization algorithm determines the magnitude of the input pressure P_{input} , the pressurization time T_{input} and the length of the four tubes in the array, L_i . For each target response we report the evolutions of curvature and pressure of the optimal system as a function of time, as obtained both numerically (solid line) and experimentally (dashed line).

radius $R = 0.38$ mm. To begin with, we also fix the top layer thicknesses of each actuator to be $t_1 = 4.0$ mm, $t_2 = 2.9$ mm, $t_3 = 2.1$ mm and $t_4 = 1.5$ mm for actuators 1, 2, 3 and 4, respectively. Consequently, the parameters to be determined by the optimization algorithm are the input pressure P_{input} , the pressurization time T_{input} and the length of

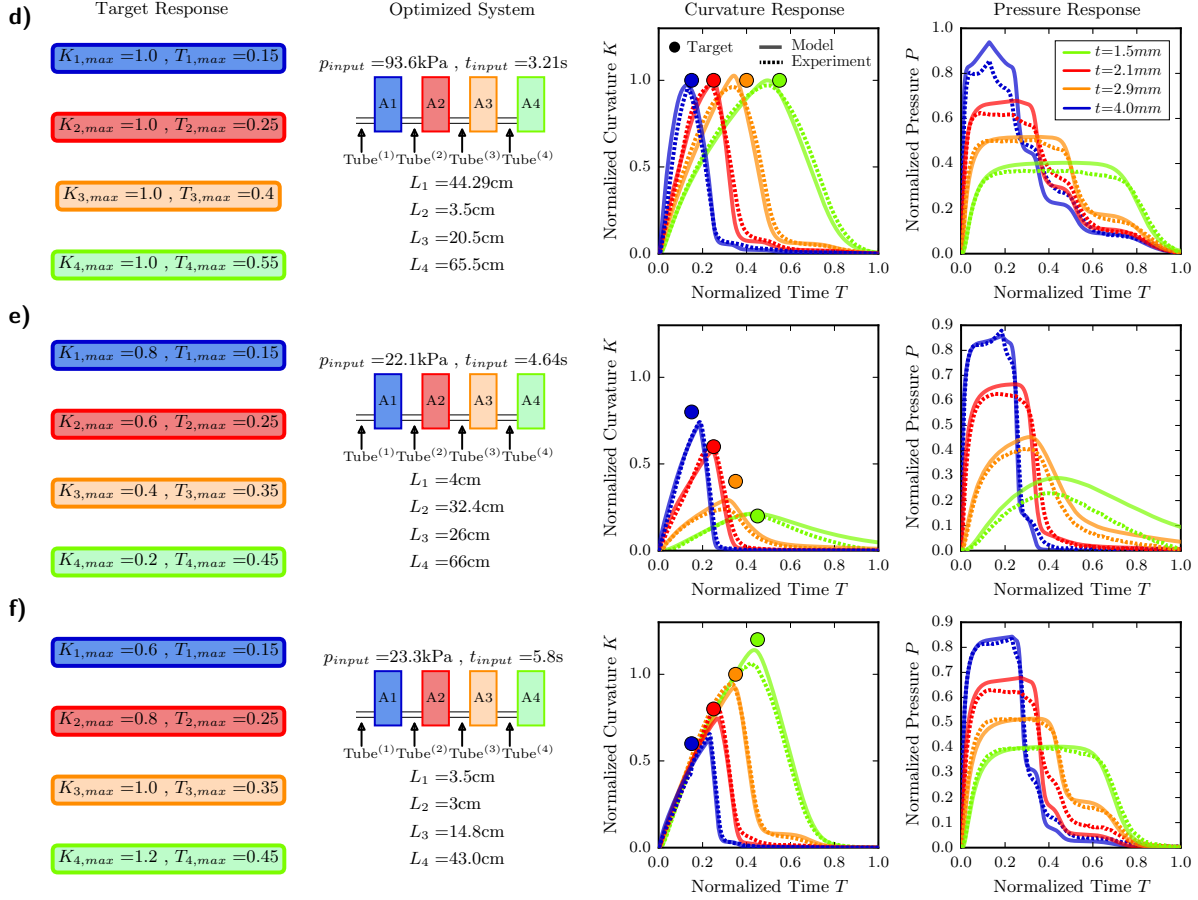


Figure S12: (Contd.) Optimal solutions to the inverse problem for a system comprising four bending actuators connected via four narrow tubes. The top layer thickness of the actuators are fixed to be $t_1 = 4.0$ mm, $t_2 = 2.9$ mm, $t_3 = 2.1$ mm and $t_4 = 1.5$ mm. The system response time is chosen as $t_{max} = 25$ sec and the tube radii are fixed to $R = 0.38$ mm. The optimization algorithm determines the magnitude of the input pressure P_{input} , the pressurization time T_{input} and the length of the four tubes in the array, L_i . For each target response we report the evolutions of curvature and pressure of the optimal system as a function of time, as obtained both numerically (solid line) and experimentally (dashed line).

each tube in the array, L_i (which can be determined from ξ_i). While in Fig. 5 of the main text we focus on two target responses, in Figs. S12 and S13 we show the results obtained solving the inverse problem for 11 different target responses, in which we vary both $K_{i,max}$ and $T_{i,max}$. For each case, we report the tube lengths L_i and pressure input parameters

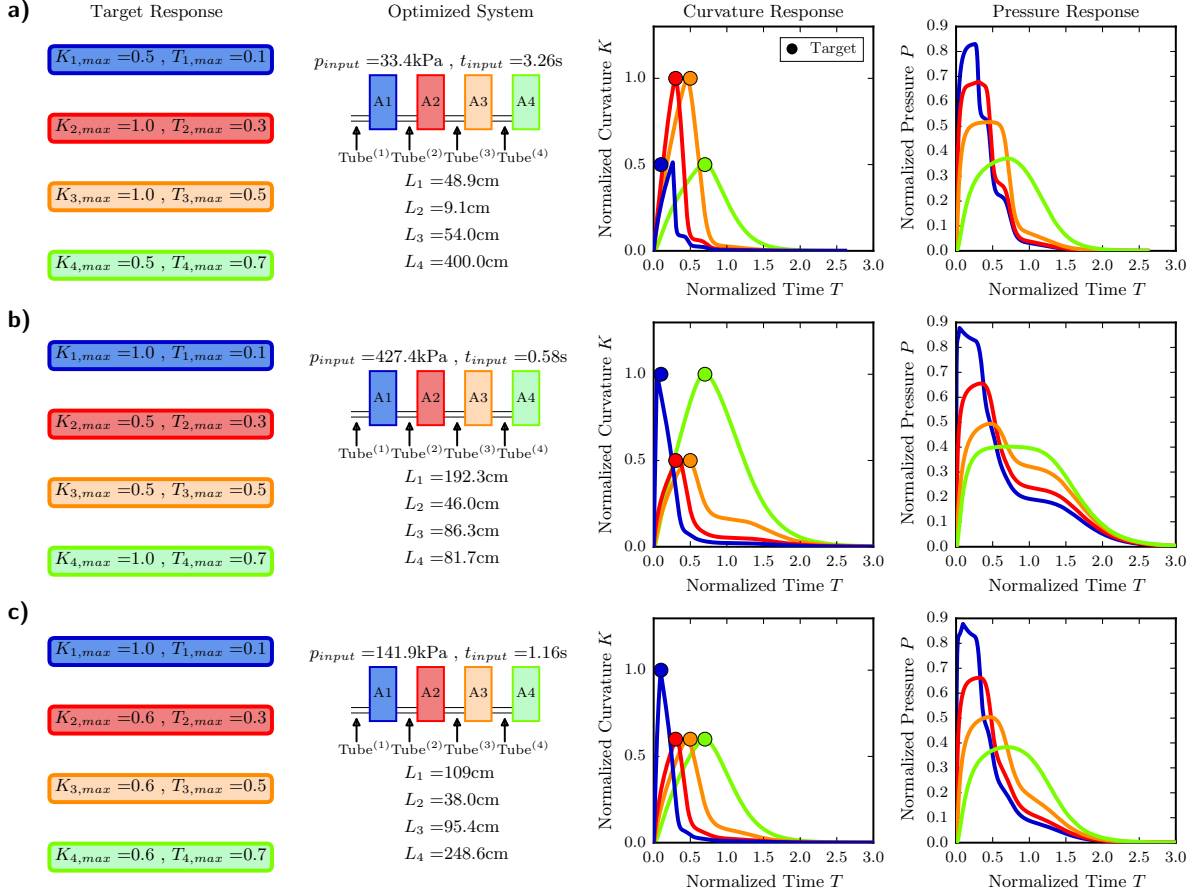


Figure S13: Optimal solutions to the inverse problem for a system comprising four bending actuators connected via four narrow tubes. The top layer thickness of the actuators are fixed to be $t_1 = 4.0 \text{ mm}$, $t_2 = 2.9 \text{ mm}$, $t_3 = 2.1 \text{ mm}$ and $t_4 = 1.5 \text{ mm}$. The system response time is chosen as $t_{max} = 25 \text{ sec}$ and the tube radii are fixed to $R = 0.38 \text{ mm}$. The optimization algorithm determines the magnitude of the input pressure P_{input} , the pressurization time T_{input} and the length of the four tubes in the array, L_i . For each target response we report the numerically obtained evolutions of curvature and pressure of the optimal system as a function of time.

P_{input} , T_{input} that correspond to the optimal solution. Moreover, for each target response we test the response of the system with the tubes and pressure input parameters determined by the optimization algorithm. For the six cases presented in Fig. S12 we test the response both numerically and experimentally, while for those reported in Fig. S13 we only perform numerical simulations. In all our tests we find a very good agreement

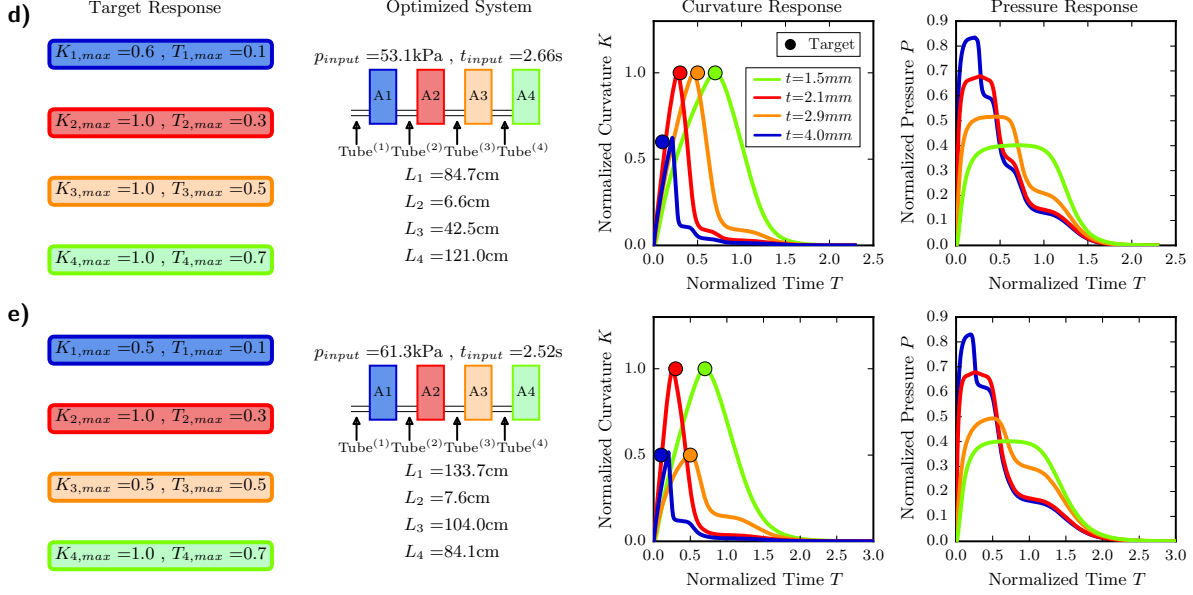


Figure S13: (Contd.) Optimal solutions to the inverse problem for a system comprising four bending actuators connected via four narrow tubes. The top layer thickness of the actuators are fixed to be $t_1 = 4.0$ mm, $t_2 = 2.9$ mm, $t_3 = 2.1$ mm and $t_4 = 1.5$ mm. The system response time is chosen as $t_{max} = 25$ sec and the tube radii are fixed to $R = 0.38$ mm. The optimization algorithm determines the magnitude of the input pressure P_{input} , the pressurization time T_{input} and the length of the four tubes in the array, L_i . For each target response we report the numerically obtained evolutions of curvature and pressure of the optimal system as a function of time.

between the curvature response and the corresponding targets. This indicates that the inverse problem formulation can successfully and very accurately identify tube lengths and pressure input parameters resulting in a wide range of target responses.

Even though the results shown in Figs. S12 and S13 indicate that a system consisting of the four bending actuators characterized by $t_1 = 4.0$ mm, $t_2 = 2.9$ mm, $t_3 = 2.1$ mm and $t_4 = 1.5$ mm can closely approach a variety of desired responses if the tubes length and inflation parameters are chosen carefully, target responses will always exist for which the optimal solution will not be a sufficiently good approximation. However, it is important to note that in such cases the solution space can be enriched by further

optimizing with respect to the top layer thicknesses of each actuator. To demonstrate that such an approach can improve the optimal solution determined by the inverse problem we consider the target response defined by $K_{i,max} = 0.8 - 0.2(i - 1)$ and $T_{i,max} = 0.15 + 0.1(i - 1)$ with $i = 1, 2, 3, 4$. If the geometry of the actuators is fixed (and characterized by $t_1 = 4.0$ mm, $t_2 = 2.9$ mm, $t_3 = 2.1$ mm and $t_4 = 1.5$ mm), we find that the system most closely matches the targets for $L_1 = 4$ cm, $L_2 = 32.4$ cm, $L_3 = 26$ cm, $L_4 = 66$ cm, $p_{input} = 22.1$ kPa. However, the numerical results reported in Fig. S14a show that for this set of parameters all four actuators fail to exactly meet the curvature anchor points, motivating the search for better performing solutions. To this end, we solve the inverse problem allowing also for the optimization of the top layer thickness, t_i , of each actuator in the array. In this case the optimization algorithm indicates that the system most closely approaches the prescribed target when the actuators are characterized by $t_1 = 3.33$ mm, $t_2 = 2.68$ mm, $t_3 = 2.8$ mm and $t_4 = 2.68$ mm, the tubes have length $L_1 = 89.3$ cm, $L_2 = 17.2$ cm, $L_3 = 4.3$ cm, $L_4 = 357.5$ cm and the inflation parameters are set to $p_{input} = 51$ kPa and $t_{input} = 1.88$ sec. The numerical results shown in Fig. S14b demonstrate that the new solution is an evident improvement to the one for which the actuators' geometry was not considered in the optimization.

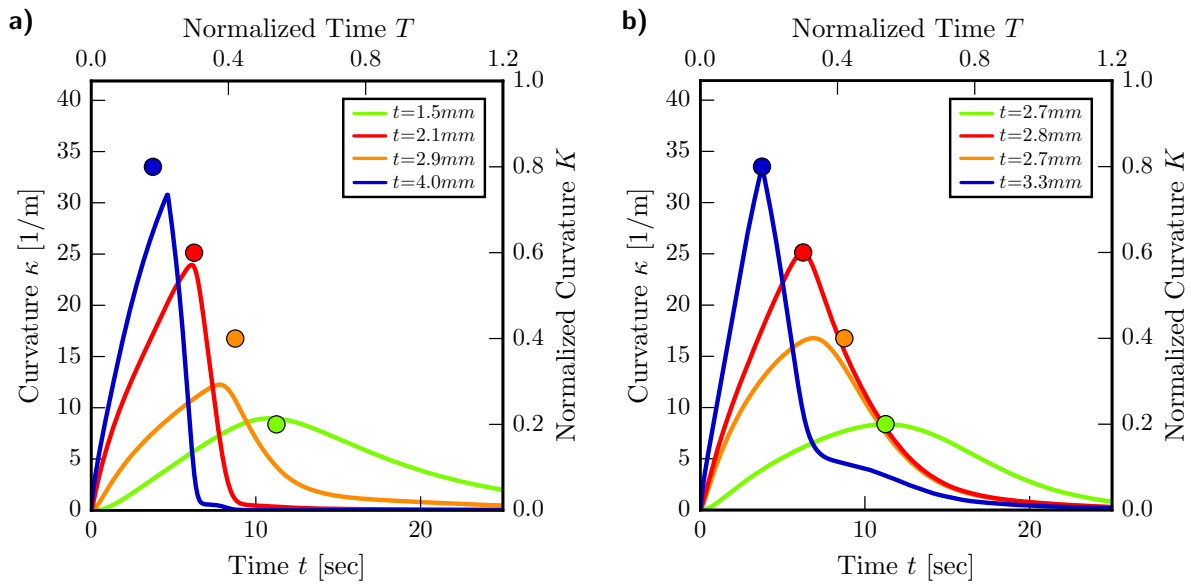


Figure S14: Allowing for the optimization of the top layer thickness of each actuator. (a) Optimal solution for the case in which the geometry of the actuators is fixed (so that the optimization algorithm only determines the tube ξ_i and inflation parameters P_{input} and T_{input}). (b) Optimal solution when the optimization also determines the top layer thickness of each actuator t_i . Note that in both cases the target target response is defined by the circular markers.

Additional Numerical Results

In this section we provide additional numerical results. In particular, Fig. S15 presents the evolution of the objective function and parameter values during optimization with CMA-ES. The results presented in Fig. S16 compare the magnitude of viscous and inviscid terms for the 3 different optimized systems presented in Fig S12.

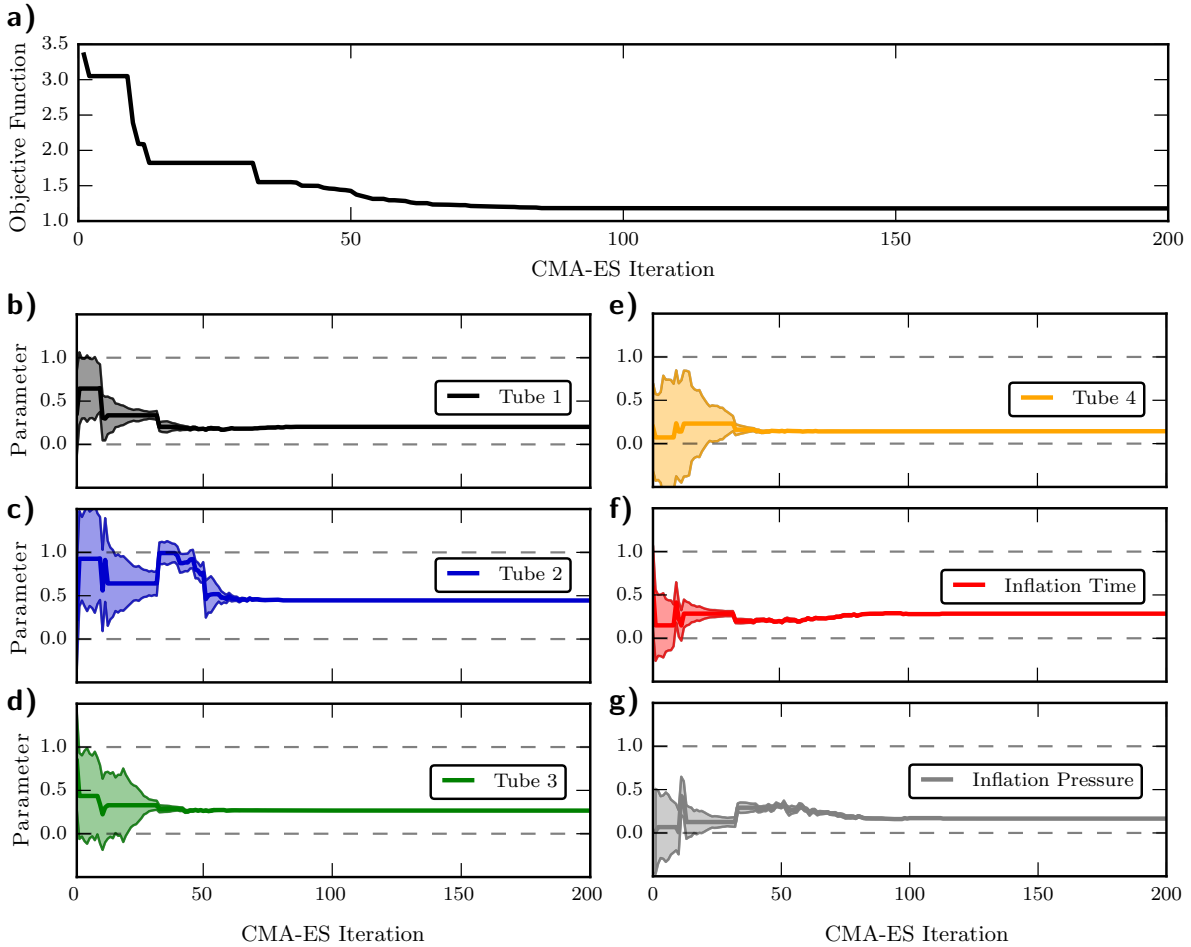


Figure S15: Optimization metrics for the case shown in Fig. S12a. (a) Evolution of the objective function during optimization with CMA-ES. (b)-(g) Evolution of the parameter values along with the standard deviation histories during optimization with CMA-ES

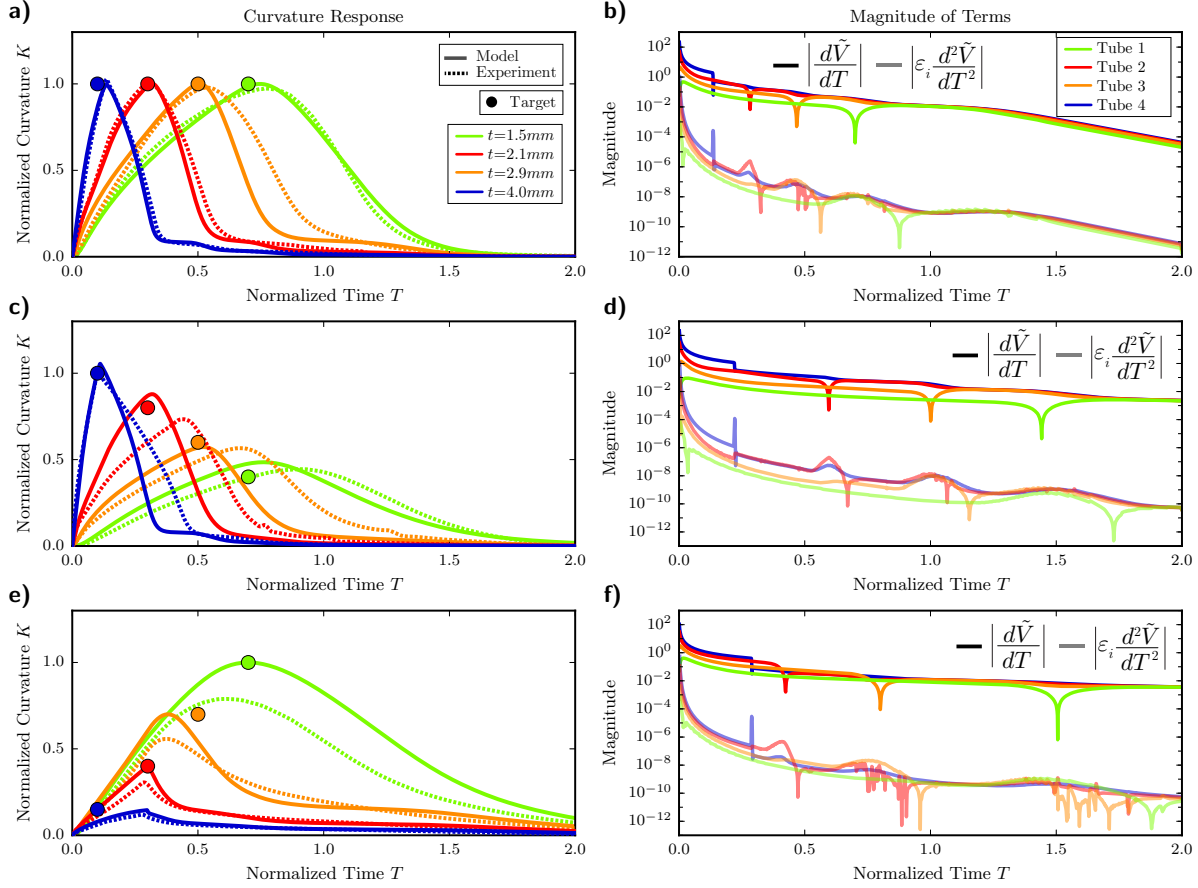


Figure S16: Comparison of the magnitude of viscous and inviscid terms for the optimized systems presented in Fig S12. (a), (c) and (e). Numerical and experimental curvature time response of the optimized systems. (b), (d) and (f) Semilog plots of the magnitude of $\varepsilon_i d^2 \tilde{V}_i / dT^2$ and $d\tilde{V} / dT$. Note that the term $\varepsilon_i d^2 \tilde{V}_i / dT^2$ effectively represents the inviscid effects in the tube, whereas $d\tilde{V} / dT$ represents the viscous effects, since in the limit where $\mu \rightarrow 0$ the term $d\tilde{V} / dT$ vanishes (i.e. no viscous contributions). The results suggest that inviscid effects are always negligible in magnitude compared to the corresponding viscous effects inside each tube. As such, the solutions presented in this work are only relevant in scenarios where viscous flow dominates.

Multi-Objective Optimization

Since soft robots are typically required to perform multiple tasks, we investigate the design of a system that can achieve two different target responses by simply changing the inflation parameters. To begin with, we focus on the optimized system shown in Fig. 5a of the main text and investigate the influence of the inflation parameters to its response by varying the inflation pressure from 0 to 320 kPa and the inflation time from 0 to 12.5 sec. To quantify the amount of deviation from the optimal solution, in Fig. S17a we report the evolution of the objective function (Eq. (7) in the main text) as a function of the input pressure and pressurization time. Moreover, in Figs. S17b-f we show the numerical (solid line) and experimental (dashed line) curvature responses corresponding to $(p_{input}, t_{input}) = (75 \text{ kPa}, 3.4 \text{ sec}), (50 \text{ kPa}, 3.4 \text{ sec}), (102 \text{ kPa}, 2.4 \text{ sec}), (102 \text{ kPa}, 1.4 \text{ sec})$ and $(102 \text{ kPa}, 3.4 \text{ sec})$. Our results suggest that changes in the input pressure and pressurization time have the ability to alter the magnitude of the curvature maxima as well as the temporal response of the system in a uniform manner. However, since the response type is highly dependent on the tubes, the responses that can be achieved just by varying the inflation parameters are quite limited.

To overcome this limitation, we formulate a multi-objective optimization problem, the solution of which corresponds to a system that can switch from one desired response (Target 1) to another (Target 2) just by varying the inflation parameters. In this case, the parameters to be determined are (a) the dimensionless tube parameters ξ_i (with $i = 1, 2, 3, 4$); (b) the magnitude of the input pressure $P_{input}^{(1)} = p_{input}^{(1)}/G$ and the pressurization time $T_{input}^{(1)} = t_{input}^{(1)}/t_{max}$ that will actuate the system towards the first target response and (c) the magnitude of the input pressure $P_{input}^{(2)} = p_{input}^{(2)}/G$ and the pressurization time $T_{input}^{(2)} = t_{input}^{(2)}/t_{max}$ that will actuate the system towards the second target response. In

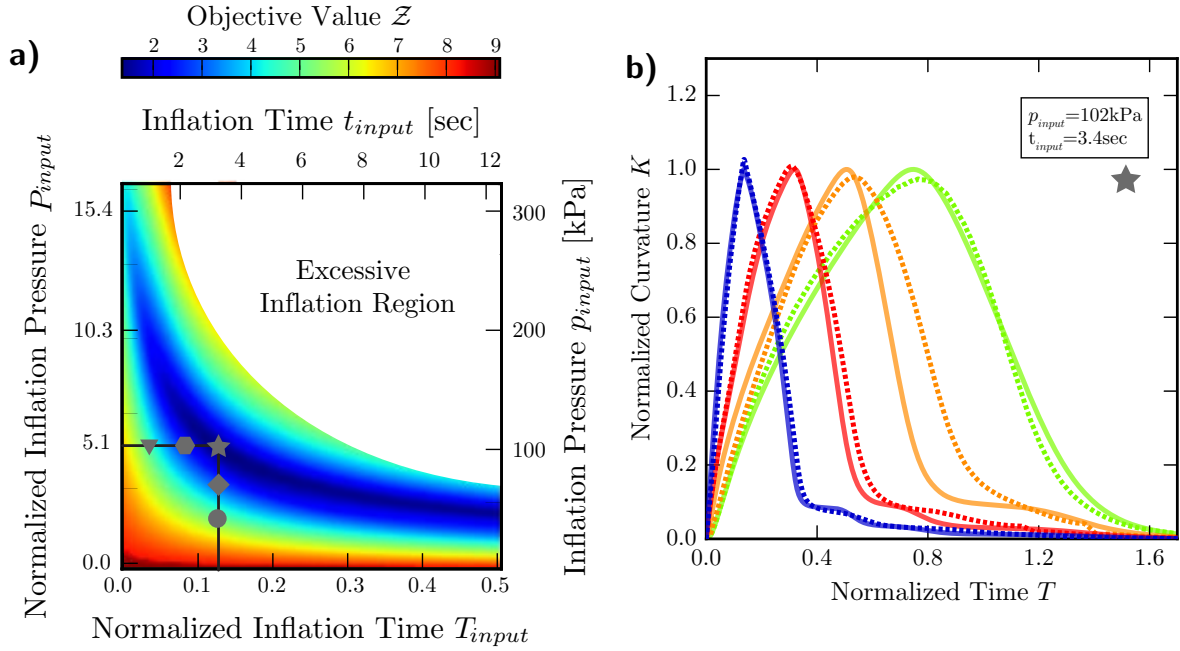


Figure S17: Influence of P_{input} and T_{input} on the response of an optimized system. The system considered here comprises four actuators characterized by $t_1 = 4.0$ mm, $t_2 = 2.9$ mm, $t_3 = 2.1$ mm and $t_4 = 1.5$ mm and connected by tubes with lengths $L_1 = 78.6$ cm, $L_2 = 10$ cm, $L_3 = 43$ cm and $L_4 = 122$ cm. This system was optimized to achieve $K_{i,max} = 1.0$ at $T_{i,max} = 0.1 + (i-1)0.2$ (with $i = 1, 2, 3, 4$). (a) Evolution of the objective function Z as a function of the input pressure magnitude P_{input} and pressurization time T_{input} . (b)-(f) Experimental (dashed lines) and numerical (solid lines) curvature responses corresponding to (b) $p_{input} = 102$ kPa and $t_{input} = 3.39$ sec (note that these are the inflation parameters obtained solving the inverse problem)

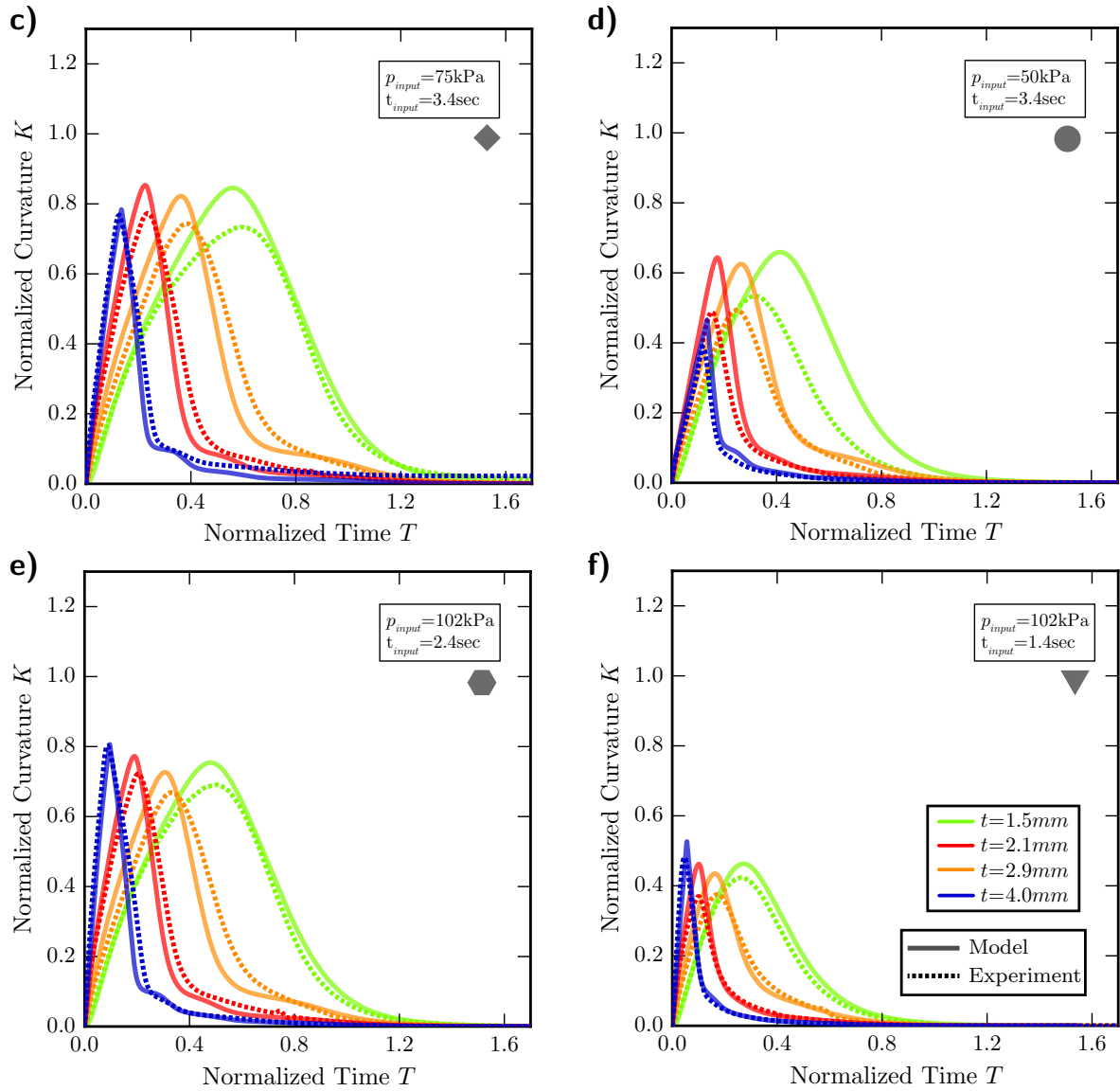


Figure S17: (Contd.) (c) $p_{input} = 75 \text{ kPa}$ and $t_{input} = 3.39 \text{ sec}$, (d) $p_{input} = 50 \text{ kPa}$ and $t_{input} = 3.39 \text{ sec}$, (e) $p_{input} = 102 \text{ kPa}$ and $t_{input} = 2.4 \text{ sec}$ and (f) $p_{input} = 102 \text{ kPa}$ and $t_{input} = 1.4$

Fig. S18 we report results for a system that can achieve two target responses defined by

$$K_{i,max}^{(1)} = 1.0 - (i - 1)0.2, \quad T_{i,max}^{(1)} = 0.1 + (i - 1)0.2 \quad (\text{S62})$$

$$K_{i,max}^{(2)} = 0.1 + (i - 1)0.3, \quad T_{i,max}^{(2)} = 0.1 + (i - 1)0.2 \quad (\text{S63})$$

with $i = 1, 2, 3, 4$. To identify the set of optimal parameters we minimize,

$$\mathcal{Z} = \alpha \mathcal{Z}^{(1)} + (1 - \alpha) \mathcal{Z}^{(2)} \quad (\text{S64})$$

where $\alpha \in [0, 1]$ is a scalar parameter weighing the relative importance of the two objectives and $\mathcal{Z}^{(1)}$, $\mathcal{Z}^{(2)}$ are the objective functions corresponding to the first and second target response, which are defined as

$$\mathcal{Z}^{(1)} = \sum_{i=1}^4 \left(\sqrt{(\Delta K_i^{(1)})^2 + (\Delta T_i^{(1)})^2} + w \tau_i \right), \quad (\text{S65})$$

$$\mathcal{Z}^{(2)} = \sum_{i=1}^4 \left(\sqrt{(\Delta K_i^{(2)})^2 + (\Delta T_i^{(2)})^2} + w \tau_i \right). \quad (\text{S66})$$

The multi-objective inverse problem is again solved using CMA-ES (with the same parameters used for the single-objective optimization). We find that the system closely approaches both objectives for $\alpha = 0.5$ when $(L_1, L_2, L_3, L_4) = (16.5, 10, 48, 124)$ cm, $p_{input}^{(1)} = 39.6$ kPa, $t_{input}^{(1)} = 6.32$, $p_{input}^{(2)} = 58.5$ kPa and $t_{input}^{(2)} = 3.33$ sec. In Figs. S18d and e we compare the numerically obtained curvature response of the system when inflated using the optimal pressure input (shown in Figs. S18f and g) to the target curvature anchor points. The results indicate that the optimal solution of the multi-objective problem closely approaches both target responses.

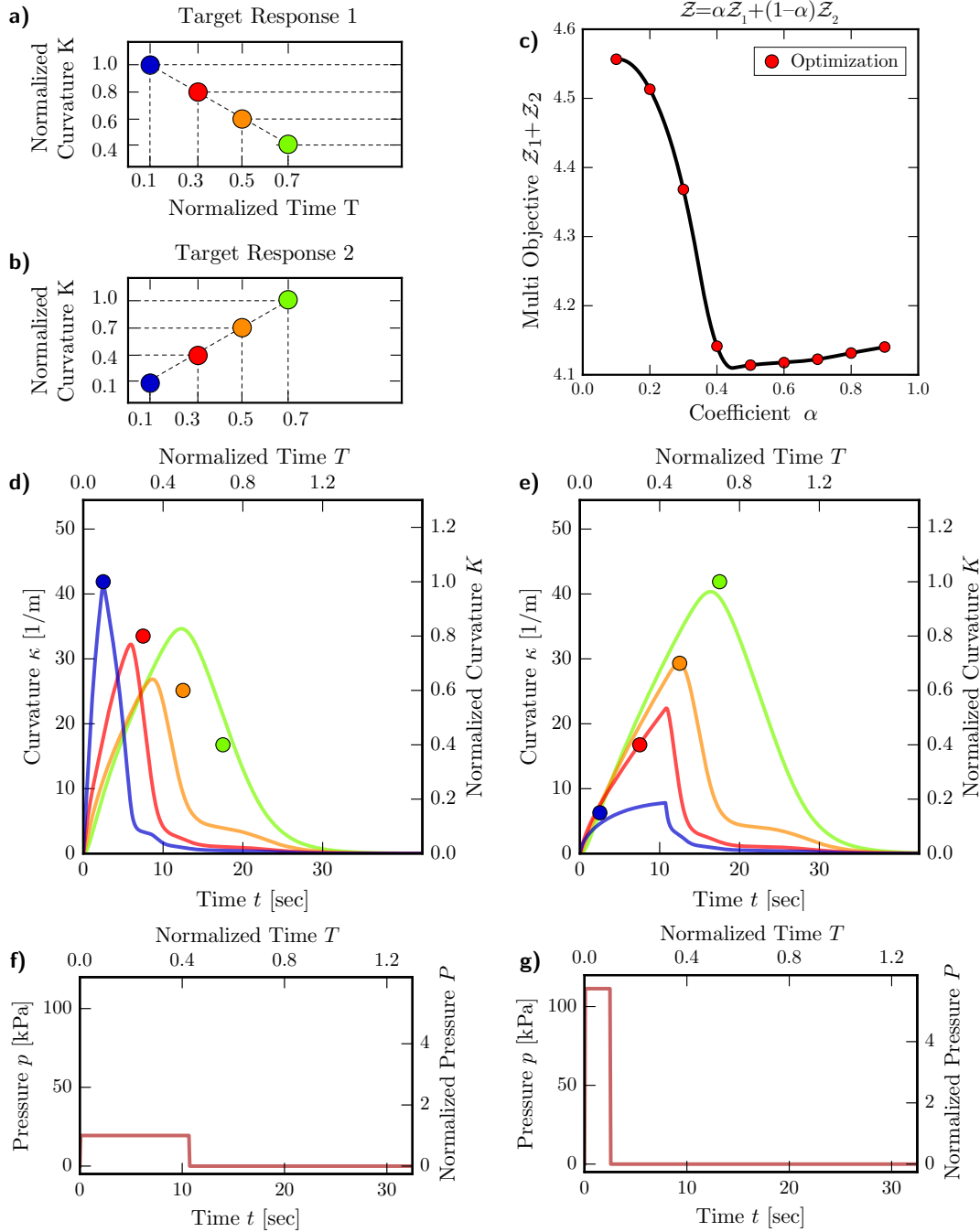


Figure S18: Multi-objective Optimization. (a)-(b) Curvature anchor points defining the first and second target response. (c) Evolution of the of $\min(Z_1 + Z_2)$ as a function of α . (d)-(e) Numerically obtained curvature-time response of the optimal system for $\alpha = 0.5$. (f)-(g) Optimal input pressure required for the system to match the first and second target response, respectively.

Supplementary References

- S1. Gent AN. A new constitutive relation for rubber. *Rubber Chem Technol* 1996;69:59–61.
- S2. Ogden RW. *Non-linear Elastic Deformations*. Chichester: E. Horwood, New York, 1984.
- S3. Kundu PK, Cohen IM, Dowling DR. (Eds). *Fluid Mechanics*, 6th Edition. Boston, MA: Academic Press, 2016.
- S4. Batchelor GK. *An Introduction to Fluid Dynamics*. Cambridge, United Kingdom: Cambridge University Press, 2000.
- S5. Pfitzner J. Poiseuille and his law. *Anaesthesia* 1976;31: 273–275.